

# High resolution, annual maps of field boundaries for smallholder-dominated croplands at national scales

Lyndon D. Estes\*<sup>1</sup>, Su Ye<sup>1,2</sup>, Lei Song<sup>1</sup>, Boka Luo<sup>1,3</sup>, J. Ronald Eastman<sup>1,3</sup>, Zhenhua Meng<sup>1</sup>, Qi Zhang<sup>1</sup>, Dennis McRitchie<sup>4</sup>, Stephanie R. Debats<sup>4</sup>, Justus Muhando<sup>5</sup>, Angeline H. Amukoa<sup>5</sup>, Brian W. Kaloo<sup>5</sup>, Jackson Makuru<sup>5</sup>, Ben K. Mbatia<sup>5</sup>, Isaac M. Muasa<sup>5</sup>, Julius Mucha<sup>5</sup>, Adelide M. Mugami<sup>5</sup>, Judith M. Mugami<sup>5</sup>, Francis W. Muinde<sup>5</sup>, Fredrick M. Mwawaza<sup>5</sup>, Jeff Ochieng<sup>5</sup>, Charles J. Oduol<sup>5</sup>, Puren Oduor<sup>5</sup>, Thuo Wanjiku<sup>5</sup>, Joseph G. Wanyoike<sup>5</sup>, Ryan B. Avery<sup>6</sup>, Kelly K. Caylor<sup>6,7,8</sup>,

<sup>1</sup>Graduate School of Geography, Clark University, Worcester, MA, USA

<sup>2</sup>Department of Natural Resources and the Environment, University of Connecticut, Storrs, CT, USA

<sup>3</sup>Clark Labs, Clark University, Worcester, MA, USA

<sup>4</sup>Independent contributor

<sup>5</sup>SpatialCollective, Nairobi, Kenya

<sup>6</sup>Department of Geography, University of California Santa Barbara, Santa Barbara, CA, USA

<sup>7</sup>Earth Research Institute, University of California Santa Barbara, Santa Barbara, CA, USA

<sup>8</sup>Bren School of Environmental Science and Management, University of California Santa Barbara, Santa Barbara, CA, USA

\* corresponding author: [lestes@clarku.edu](mailto:lestes@clarku.edu)

This pre-print is a revised version of a manuscript that has undergone one round of peer review in *Frontiers in Artificial Intelligence*, where it has been resubmitted. This version will be updated as it is further revised, and the final published version will be accessible through its DOI link.

---

## Abstract

Mapping the characteristics of Africa’s smallholder-dominated croplands, including the sizes and numbers of fields, can provide critical insights into food security and a range of other socioeconomic and environmental concerns. However, accurately mapping these systems is difficult because there is 1) a spatial and temporal mismatch between satellite sensors and smallholder fields, and 2) a lack of high-quality labels needed to train and assess machine learning classifiers. We developed an approach designed to address these two problems, and used it to map Ghana’s croplands. To overcome the spatio-temporal mismatch, we converted daily, high resolution imagery into two cloud-free composites (the primary growing season and subsequent dry season) covering the 2018 agricultural year, providing a seasonal contrast that helps to improve classification accuracy. To address the problem of label availability, we created a platform that rigorously assesses and minimizes label error, and used it to iteratively train a Random Forests classifier with active learning, which identifies the most informative training sample based on prediction uncertainty. Minimizing label errors improved model F1 scores by up to 25%. Active learning increased F1 scores by an average of 9.1% between first and last training iterations, and 2.3% more than models trained with randomly selected labels. We used the resulting 3.7 m map of cropland probabilities within a segmentation algorithm to delineate crop field boundaries. Using an independent map reference sample (n=1,207), we found that the cropland probability and field boundary maps had respective overall accuracies of 88% and 86.7%, user’s accuracies for the cropland class of 61.2% and 78.9%, and producer’s accuracies of 67.3% and 58.2%. An unbiased area estimate calculated from the map reference sample indicates that cropland covers 17.1% (15.4-18.9%) of Ghana. Using the most accurate validation labels to correct for biases in the segmented field boundaries map, we estimated that the average size and total number of field in Ghana are 1.73 ha and 1,662,281, respectively. Our results demonstrate an adaptable and transferable approach for developing annual, country-scale maps of crop field boundaries, with several features that effectively mitigate the errors inherent in remote sensing of smallholder-dominated agriculture.

31

---

## 1 Introduction

32

33 Amidst all the challenges posed by global change, a particular concern is how agricultural systems will  
34 adapt to meet humanity’s growing food demands, and the impacts that transforming and expanding  
35 food systems will have on societies, economies, and the environment (Searchinger et al. 2019). A  
36 number of efforts are underway to address various aspects of this challenge, including work on  
37 diagnosing and closing yield gaps (Lobell et al. 2009, e.g. Licker et al. 2010, Mueller et al. 2012),  
38 expanding and commercializing production (Morris and Byerlee 2009), and to understand (Rulli and  
39 D’Odorico 2014, Kehoe et al. 2017, Davis et al. 2020) and mitigate (Estes et al. 2016b) agriculture’s  
40 ecological impacts. The success of these efforts depends heavily on data that accurately describes the  
41 location and characteristics of croplands (Fritz et al. 2015), and, given the rapid pace of agricultural  
42 change (Gibbs et al. 2010, Zeng et al. 2018, Bullock et al. 2021), how these are changing from one year

43 to the next. Unfortunately, for many regions, existing cropland datasets are inaccurate, and are usually  
44 created as once-off or infrequently updated products. As such, estimates of global cropland area tend to  
45 vary widely, often disagree about where croplands are located (e.g. Fritz et al. 2011, 2013), and become  
46 rapidly outdated. Errors in these maps can propagate in subsequent analyses that use cropland data as  
47 inputs, resulting in potentially misleading answers (Estes et al. 2018). Beyond distributions, few data  
48 are available on key cropland characteristics such as field size, an important variable needed to estimate  
49 yield and other key food security variables (Carletto et al. 2015), and as an indicator of farm size  
50 (Levin 2006, Samberg et al. 2016), a critical component of rural livelihoods given increasing population  
51 densities and longstanding debates about the relationship between farm size and productivity (Feder  
52 1985, Carletto et al. 2013, Desiere and Jolliffe 2018).

53 The deficit of information is due to the fact that in many regions the only source of cropland data are  
54 remotely sensed land cover maps, which are prone to error. This is particularly true in Africa (Fritz et  
55 al. 2010, Estes et al. 2018), where agricultural changes will be largest and the need for accurate  
56 baseline data is thus greatest (Searchinger et al. 2015, Estes et al. 2016b, Bullock et al. 2021), and  
57 where the characteristics of croplands exacerbate the error inherent in remote sensing analyses. Half of  
58 all fields in Africa’s smallholder-dominated agricultural systems are smaller than 1 ha (Lesiv et al.  
59 2019). This size is small relative to the 30-250 m resolution of the sensors typically used in many  
60 landcover mapping efforts (e.g. Chen et al. 2015, Sulla-Menashe et al. 2019), which results in errors due  
61 to mixed pixels and aspects of the modifiable area unit problem (Openshaw and Taylor 1979, Boschetti  
62 et al. 2004), wherein the pixel’s shape does not match that of crop fields, and is too coarse to aggregate  
63 into an approximation of that shape (Dark and Bram 2007, Estes et al. 2018). On top of the matter of  
64 scale is the high variability within and between fields, their tendency to intergrade with surrounding  
65 vegetation (Debats et al. 2016, Estes et al. 2016a), and the high temporal variability within croplands.  
66 These last three aspects pose challenges for the classification algorithms that are applied to the imagery.

67 Recent technological advances are helping to overcome these challenges. Chief among these are the  
68 growing numbers of satellites that collect high (<5 m) to near-high (10 m) resolution imagery at  
69 sub-weekly intervals (Drusch et al. 2012, McCabe et al. 2017). The spatial resolution of these imagery  
70 addresses the scale mismatch between sensor and field, and their high frequency captures the seasonal  
71 dynamics of cropland, which helps classifiers distinguish cropland from surrounding cover types (Debats

72 et al. 2016, Defourny et al. 2019). On top of this, the opening of satellite image archives (Wulder et al.  
73 2016) and advances in cloud computing are placing large volumes of moderate to near-high resolution  
74 imagery together with the computational and algorithmic resources necessary to classify them at scale  
75 (Gorelick et al. 2017). These capabilities have already been used to create a new generation of higher  
76 resolution (10-30 m) cropland and landcover maps for Africa and other regions [ESA (n.d.); Lesiv et al.  
77 (2017); Xiong et al. (2017); (Zhang et al. 2021)]. However, the potential of the highest resolution (<5  
78 m) imagery to map cropland over very large extents (e.g. country scales) has yet to be realized,  
79 presumably because these data are commercial and relatively expensive, and require significant  
80 computational resource to process.

81 Beyond the imagery and computational gains, machine learning algorithms are rapidly advancing,  
82 providing large gains in classification performance (Maxwell et al. 2018, Ma et al. 2019). However, the  
83 ability to take advantage of these gains is often limited by newer models' need for large training  
84 datasets, which are typically unavailable, hard to collect, or contain numerous errors (Ma et al. 2019,  
85 Elmes et al. 2020, Burke et al. 2021). To build sufficient training samples, as well as the reference data  
86 needed to objectively assess their performance (we refer collectively to both types as "labels,"  
87 distinguishing between each as needed), map-makers rely heavily on visual interpretation of high  
88 resolution satellite or aerial imagery (Chen et al. 2015, e.g. Xiong et al. 2017, Stehman and Foody  
89 2019), as it is impractical and expensive to collect these data in the field over large areas, particularly  
90 on an ongoing basis. Consequently, a number of web-based platforms have been developed to collect  
91 such labels (Fritz et al. 2012, Estes et al. 2016a, e.g. Bey et al. 2016). Image-drawn labels present two  
92 particular problems. The first is that they inevitably contain errors of interpretation, which can vary  
93 substantially according to the skill of the labeller, particularly over complex croplands with small field  
94 sizes (Estes et al. 2016a, Waldner et al. 2019). The second problem is that visual interpretation  
95 depends on high resolution imagery (<5 m), as fields are increasingly difficult to discern as image  
96 resolution decreases. Typically the only available source of high resolution imagery is "virtual globe"  
97 basemaps (e.g. Bing or Google Maps), which present mosaics of high resolution satellite and aerial  
98 images collected over a span of several years (Lesiv et al. 2018). This within-mosaic temporal variation  
99 can create a temporal mismatch between the labels and the imagery being classified, which is usually  
100 from a different source (e.g. Landsat, Sentinel; Xiong et al. (2017)). If a land change occurs in the

101 interval between the two image sets (e.g. a new field was created), the label, even if accurately drawn,  
102 introduces error into the classifier. This source of error may be elevated in croplands where swidden  
103 agriculture is practiced (Van Vliet et al. 2013), or in rapidly developing agricultural frontiers (Zeng et  
104 al. 2018). Despite the high potential for it, label error is often not considered during model training  
105 and map accuracy assessment, resulting not only in the potential for maps to be misused or  
106 misinterpreted, but in missed opportunities to improve model performance (Estes et al. 2018, Stehman  
107 and Foody 2019, Elmes et al. 2020).

108 Taking into consideration the advances and remaining limitations described above, the ability to map  
109 smallholder-dominated croplands can be further improved by 1) more fully exploiting the profusion of  
110 high frequency, high resolution imagery provided by CubeSats (McCabe et al. 2017), and 2) by  
111 implementing methods that improve the ability to collect and minimize errors in image-interpreted  
112 labels. We developed a mapping approach that focuses on these two sources of improvement. Our  
113 approach uses PlanetScope imagery collected by Planet’s fleet of Dove satellite, which provides 3-4 m  
114 resolution imagery over large areas at near daily intervals (McCabe et al. 2017, PlanetTeam 2018), at  
115 relatively low to no cost for academic research<sup>1</sup> and non-commercial, sustainability-oriented  
116 applications<sup>2</sup>. Although these data are of lower spectral depth and, in some cases, quality, than  
117 Landsat, Sentinel, or Worldview imagery, their daily revisit enables country- to continent-scale image  
118 mosaics to be created for multiple periods during a single agricultural year, even over the cloudiest  
119 forest regions where it is hard to successfully construct cloud-free composites from optical imagery with  
120 return intervals (even by a few days). This ability to capture intra-annual variability can be more  
121 important for classifying cropland than spectral depth (Debats et al. 2016). Beyond the frequency,  
122 PlanetScope’s 3.7 m resolution—although substantially coarser than the 0.5-1 m imagery available in  
123 most areas covered by virtual globes—is sufficiently resolved for humans to discern small fields under  
124 many conditions (Fourie 2009, e.g. see Estes et al. 2018). This allows labels to be made using the same  
125 imagery that is classified, which helps to minimize label error. To further reduce label noise, we  
126 developed a platform that includes rigorous label accuracy assessment protocols and a novel approach  
127 for creating consensus labels, which helps reduce mistakes made by individual labellers (Estes et al.  
128 2016a, Elmes et al. 2020). We couple the labelling platform with a machine learning model inside an

---

<sup>1</sup>[www.planet.com/markets/education-and-research/](http://www.planet.com/markets/education-and-research/)

<sup>2</sup>[assets.planet.com/docs/Planet\\_ParticipantLicenseAgreement\\_NICFI.pdf](https://assets.planet.com/docs/Planet_ParticipantLicenseAgreement_NICFI.pdf)

129 active learning (Cohn et al. 1994, Tuia et al. 2011) framework, in which the model is trained  
130 interactively, using the model’s prediction uncertainty over unlabelled areas to select new sites for  
131 additional labelling (Cohn et al. 1994, Tuia et al. 2011). This approach helps boost the performance of  
132 the classifier while reducing the overall number of labels required to achieve a given level of performance  
133 (Debats et al. 2017, e.g. Hamrouni et al. 2021). An unsupervised segmentation step is then applied to  
134 convert pixel-wise cropland predictions into vectorized maps of individual field boundaries.

135 Here we use this approach to create a high resolution, country-scale map of crop field boundaries in  
136 Ghana, a country where smallholder farming predominates across a broad mix of climate and  
137 agricultural systems, ranging from primarily grain and vegetable crop production in the northern  
138 savannas to tree crop-dominated systems in the forested southwest, including large areas where shifting  
139 agriculture is practiced (Samberg et al. 2016, Kansanga et al. 2019). The map represents a single  
140 agricultural year (2018-2019), as opposed to a multi-year epoch, thereby demonstrating a capacity for  
141 annual, high resolution maps that can be used to monitor rapidly evolving small-scale agricultural  
142 systems, including key characteristics such as field size. In addition to providing valuable new data and  
143 insight into Ghana’s agriculture, our study demonstrates one of the most spatially extensive  
144 agricultural applications of CubeSats to date, provides a new technique for converting daily imagery  
145 into seasonal composites, and shows how best practices for model training and label collection can be  
146 applied to improve map accuracy (Elmes et al. 2020).

## 147 **2 Materials and Methods**

148 The mapping approach we developed is comprised of four open source components (Figure 1) that are  
149 designed to run in a cloud computing environment. The first component collects daily PlanetScope  
150 imagery and converts them into cloud-free seasonal composites. The second is a custom-built platform  
151 that provides tools for labelling the composites, along with procedures to assess and minimize label  
152 error. This platform interacts with the third component, a machine learning process, within an active  
153 learning (Cohn et al. 1994, Tuia et al. 2011) loop, to produce a map of predicted cropland probabilities  
154 for each image pixel. The fourth and final component is an algorithm that segments the image  
155 composites, then filters the resulting polygons using the pixel-wise cropland predictions produced by  
156 the active learning classifier, resulting in a final set of vectorized field boundaries.

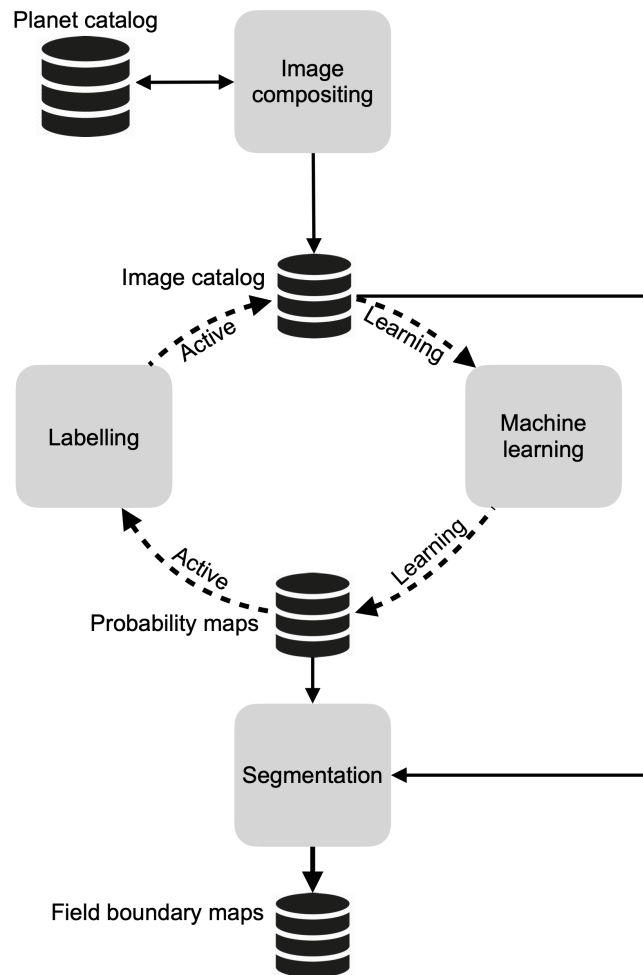


Figure 1: An overview of the primary mapping components, the data stores that hold the inputs and outputs from each component, and the direction of connections between them. The dashed line indicates iterative interactions, while solid lines indicate one-time or irregular connections.

157 We describe each component in further detail in the following section, and how we applied them to map  
158 Ghana’s annual cropland boundaries, excluding tree crops.

## 159 **2.1 Image compositing**

160 The image processing component was designed for PlanetScope Analytic surface reflectance imagery  
161 (PlanetTeam 2018), which provides three visual (red, green, blue) and near-infrared bands at 3.7 m  
162 resolution at nominal daily frequency. The images are provided as ortho-rectified and converted to  
163 surface reflectance, although there are residual errors from inter-sensor differences and the radiometric  
164 normalization process (Houborg and McCabe 2018), variation in the orientation of scene footprints, as  
165 well as a high frequency of cloud cover over the study region (Wilson and Jetz 2016, Roy et al. 2021)  
166 that are not fully captured by the provided cloud masks. To minimize the effect of these residual errors,  
167 we developed a procedure for creating temporal composites of the primary growing and non-growing  
168 seasons within a single 12-month period. For Ghana, we defined the primary growing season as May  
169 through September, followed by the off (or dry) season from November or December through February.  
170 We chose these two seasons because prior work shows that the contrast between them improves  
171 cropland classifications (Debats et al. 2016), Furthermore, capturing the seasons in this sequence  
172 during the same year helps minimize differences caused by land change. The wide time intervals we  
173 used to define each season were necessary for collecting a sufficient number of images to make high  
174 quality composites, as Ghana’s cloud cover renders many scenes unusable and therefore unavailable in  
175 Planet’s catalog, thus the effective return interval can be substantially longer than 24 hours during the  
176 cloudiest months (Roy et al. 2021).

177 We collected all available scenes intersecting Ghana and falling within these two seasons during the  
178 2018 agricultural year (defined here as March, 2018-February, 2019) via the Planet API (PlanetTeam  
179 2018), and transferred these to cloud storage (Amazon Web Services [AWS] S3). We then converted  
180 each scene into analysis ready data (Dwyer et al. 2018) by cropping each to the boundaries of a  $0.05^\circ$   
181 grid that it intersected (see Figure S1 in Supplemental Information [SI]), which provided the  
182 dimensions for making composited image tiles. We chose this cell size for tiling because it is slightly  
183 narrower than the short axis of a PlanetScope scene, which increases the number of intersecting scenes  
184 that completely cover the tile, thereby helping to minimize edge artifacts in the composites.



185 To create a seasonal composite, we calculated two weights for the time series of each pixel within the  
 186 ARD stack for a given season:

$$W1_t = \frac{1}{blue_t^2} \quad (1)$$

$$W2_t = \begin{cases} \frac{1}{NIR_t^4}, & \text{if } NIR_t < \text{median}\{NIR_{t1}, NIR_{t2}, \dots, NIR_{ti}\}. \\ 1, & \text{otherwise.} \end{cases} \quad (2)$$

187 Where  $t$  is a particular date in the pixel time series, which begins at date 1 for the given compositing  
 188 period and ends on date  $i$ ,  $blue$  is the blue band, and  $NIR$  the near infrared band. Equation 1 assigns  
 189 lower weights to hazy and clouded pixels as the blue band is sensitive to these atmospheric features  
 190 (Zhang et al. 2002), while Equation 2 assigns low weights to pixels in cloud shadow (Zhu and  
 191 Woodcock 2012, Qiu et al. 2020)

192 After assigning these two weights, we calculated the final composited pixel value:

$$\bar{B} = \frac{\sum_{t=1}^T B_t * W1_t * W2_t}{\sum_{t=1}^T W1_t * W2_t} \quad (3)$$

193 Which is the weighted mean for each pixel for each band  $B$  for the given season.

194 Each composited seasonal tile was saved as a cloud-optimized geotiff, and a “slippy map<sup>3</sup>” rendering  
 195 was created for each composite using Raster Foundry (Azavea 2020), for display within the labelling  
 196 platform (next section).

197 We generated a catalog of 16232 composite tiles (hereafter simply “tiles”) for Ghana, consisting of a  
 198 seasonal pair for each of the 8116  $0.05^\circ$  tile grid cells covering Ghana. To assess the quality of the  
 199 resulting composites, 50 tile grid cells were randomly selected, and two separate observers graded each  
 200 corresponding seasonal composite using four categories that evaluated the degree of 1) residual cloud

<sup>3</sup>[https://wiki.openstreetmap.org/wiki/Slippy\\_Map](https://wiki.openstreetmap.org/wiki/Slippy_Map)

201 and 2) cloud shadow, 3) the number of visible scene boundary artifacts, and 4) the proportion of the  
202 image with resolution degraded below the 3.7 m PlanetScope resolution (e.g. because of between-date  
203 image mis-registrations). Each category was qualitatively ranked from 0-3, with 0 being the lowest  
204 quality, and 3 the highest (see SI for complete protocol), making the highest possible score 12. We  
205 rescaled scores to fall between 0 and 1.

## 206 **2.2 Mapping cropland probabilities with active learning**

207 The first step in creating a country-wide field boundary map of Ghana was to create a pixel-wise  
208 classification of cropland probabilities throughout the country. Given the high resolution of the imagery  
209 and the need to minimize the computational burden, we divided Ghana into 16 distinct mapping  
210 regions, or Areas of Interest (AOIs). We constructed the AOIs by grouping together tile grids into  
211 blocks representing the larger 1° cells used to assign tile identifiers (Figure S1A). We grouped tile cells  
212 from 1° degree cells that overlapped Ghana’s boundaries together with those from the nearest 1° cell  
213 contained entirely within Ghana (with the exception of AOI 16, which was comprised of tile grids from  
214 the 1° cells along Ghana’s southern coast. The average extent of the resulting AOIs was 15,457 km<sup>2</sup>  
215 (range 12,160-23,535 km<sup>2</sup>).

216 We used the active learning process to develop a separate cropland classification model for each of these  
217 AOIs, based on an approach described by Debats et al (2017). We initiated the process by training a  
218 starter model using labels from a set of randomly selected training sites drawn from a 0.005° grid that  
219 was nested within the tiling grid. This finer grid, which we refer to as the “primary grid” for simplicity,  
220 provided the target area for creating labels (section 2.2.1), as well as the unit for distributing  
221 computing jobs (section 2.2.2). We then assessed the performance of the starter model against a  
222 separate set of validation labels developed for each AOI, applied the model to predict cropland  
223 probabilities for pixels in unlabelled primary grid cells in each AOI, and calculated an uncertainty  
224 criterion (Debats et al. 2017):

$$Q_I = \sum_{I(x,y) \in I} (p(x,y) - 0.5)^2 \quad (4)$$

225 Where  $Q$  is the uncertainty for each unlabelled primary grid cell  $I$ , calculated from the predicted  
226 probability  $p$  of a randomly selected subset of pixels  $(x, y)$  drawn from it. Pixels with predicted  
227 probabilities closer to 0.5 are least certain as to their classification, thus the lowest values of  $Q$   
228 represent primary grid cells posing the most difficulty for the classifier.

229 We ranked the unlabelled primary grid cells from least to most certain, randomly selected a subset of  
230 cells from the top 30% of the ranking (to minimize the risk of spatial autocorrelation), and sent these  
231 back to the labelling platform. After these new sites were labelled, they were added to the starter pool  
232 of labels, the model was retrained with the larger training set, its performance and prediction  
233 uncertainty was reassessed, and a new sample of the most uncertain primary grid cells was again sent  
234 for labelling. This loop was typically repeated for 3 iterations, after which a final map of cropland  
235 probabilities was made.

236 In the next two sections, we describe the labelling and machine learning components of the active  
237 learning process in more detail.

### 238 **2.2.1 Labelling**

239 To collect the initial randomized samples for model training, we grouped the AOIs (Figure S1A) into  
240 three clusters based on approximate agro-ecological similarity: the 6 northernmost savanna-zone AOIs  
241 (Cluster 1), a central to southeastern cluster (Cluster 2) consisting of the 3 middle (AOIs 7-9) and 2  
242 southeastern AOIs (12 and 15), and a southwestern cluster (Cluster 3) made up of the forest zone AOIs  
243 (10, 11, 13, 14, 16). Within each cluster, we randomly selected and labelled 500 primary grid cells,  
244 which provided relatively large initial training samples for these agro-ecologically similar regions, while  
245 helping to minimize the overall amount of labelling effort. To create validation samples, we randomly  
246 selected and labelled 100 primary grid cells per AOI, and a further 100 cells were labelled in each AOI  
247 during each active learning iteration.

248 In addition to training and validation labels, we also collected training reference labels and map  
249 reference labels (Elmes et al. 2020). The former were a set of 98 primary grid cells selected to represent  
250 the range of cropland types and densities in Ghana, which were labelled by expert analysts (the lead  
251 researchers on this project). We used these to assess the performance of the individual labellers

252 collecting training and validation labels. Map reference labels were collected and used to assess the  
253 accuracy of the final map (see Section 2.4).

254 We collected all labels using a custom-built platform that we adapted from an earlier prototype we  
255 developed for crowdsourced labelling (Estes et al. 2016a). We enhanced this platform by making  
256 several major additions, including an independent backend that allowed us to recruit and manage our  
257 own labelling teams, improved procedures for assessing and improving label accuracy, and processes for  
258 automating the machine learning component. The platform runs on a cloud-hosted Linux virtual server  
259 (AWS EC2) and is comprised of a database (PostGIS/Postgres), a mapping interface (OpenLayers 3),  
260 an image server (Raster Foundry), and a set of utilities for managing, assessing, and converting  
261 digitized field boundaries into rasterized labels.

262 We created a separate labelling instance for each AOI. To create training and validation labels, labellers  
263 (the co-authors of this paper) logged into the website (built with Flask) for a particular AOI and  
264 navigated to the mapping interface (Figure 2), where they were presented with a white target box  
265 representing a primary grid cell to label, a set of digitizing tools, and several different sources of  
266 imagery. These included true and false color renderings of the growing season and dry season  
267 PlanetScope composites, and several virtual globe basemaps. They then used the polygon drawing tool  
268 to digitize the boundaries of all crop fields visible within the PlanetScope overlays that intersect the  
269 target grid cell. For this project, labellers were instructed to digitize active or recently active crop  
270 fields, avoiding tree crops, and fallow or potentially abandoned fields (see SI for digitizing rules). To aid  
271 with interpretation, labellers toggled between the PlanetScope renderings and the basemaps to help  
272 form a judgement about what constitutes a field. The labeller assigned each digitized polygon a class  
273 category (e.g. annual cropland), saved all completed fields to the database, and were then presented  
274 with the next target to label. If the target grid cell did not contain any fields, labellers simply pressed  
275 save to go to the next cell.

276 The flow of labelling targets presented to each worker was determined by the platform’s built-in  
277 scheduler. Each primary grid cell selected for labeling was placed into a queue within the platform’s  
278 database, and converted into a labelling *task* with a specified number of *assignments* (the boundaries  
279 drawn by an individual labeller) that had to be completed in order to finish the task. There were two

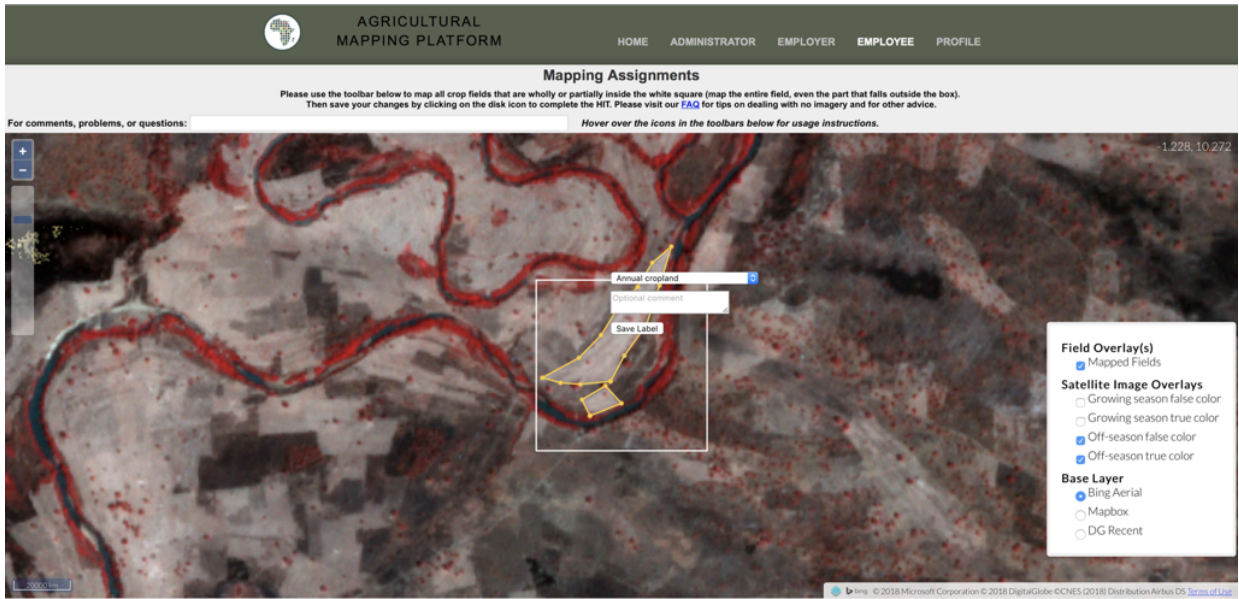


Figure 2: An overview of the labelling platform’s interface

280 types of tasks, accuracy assessment or model training/validation, with the assignments for each  
 281 indistinguishable to labellers. Upon completing an accuracy assessment assignment, the platform  
 282 invoked a scoring algorithm that compared the labeller’s digitized boundaries against a set of training  
 283 reference polygons, resulting in a label quality score:

$$\text{score}_i = \beta_0 I + \beta_1 O + \beta_2 F + \beta_3 E + \beta_4 C \quad (5)$$

284 Where  $i$  indicates the particular assignment, and  $\beta_{0-4}$  represent varying weights that sum to 1.  $I$  refers  
 285 to “inside the box” accuracy,  $O$  is the accuracy of those portions of the labeller’s polygons extending  
 286 beyond the target grid boundaries,  $F$  is fragmentation accuracy, a measure of how many individual  
 287 polygons the labeller delineated relative to the reference,  $E$  measures how closely each polygon’s  
 288 boundary matched its corresponding reference polygon boundary, and  $C$  assesses the accuracy of the  
 289 labeller’s thematic labels (see SI for individual formulae). Equation 5 is an extension of the approach  
 290 described by Estes et al. (2016).

291 We configured the platform’s scheduler to present workers with accuracy assessment assignments at a  
 292 rate of 1 for every 5 assignments mapped. This generated a history of accuracy assessment scores that

293 we used to assess label quality and minimize label error.

294 For training and validation, where there was no reference data to assess label accuracy, we set each task  
295 to have four assignments, i.e. each was completed by four separate labellers. When all four assignments  
296 were complete, a Bayesian merging routine was invoked to combine the four sets of labels into a single  
297 consensus label:

$$P(\theta|D) = \sum_{i=1}^n P(W_i|D)P(\theta|D, W_i) \quad (6)$$

298 Where  $\theta$  represents the true cover type of a pixel (field or not field),  $D$  is the label assigned to that  
299 pixel by a labeller, and  $W_i$  is an individual labeller.  $P(\theta|D)$  is the probability that the actual cover type  
300 is what the labellers who mapped it says it is, while  $P(W_i|D)$  is the average score (ranging between 0  
301 and 1) of the accuracy assessment assignments an individual labeller completed within the AOI, and  
302  $P(W\theta|D, W_i)$  is the labeller’s label for that pixel. This approach therefore used the average assignment  
303 quality score to weight each labeller’s label for a given pixel (see SI for further details). Each pixel in  
304 the target grid cell was merged using this approach ( $n = 40000$ ), which helps to minimize individual  
305 labellers’ errors. We estimated a confidence measure for each consensus label by calculating its  
306 Bayesian Risk (see SI), which ranges between 0 and 1, with 0 indicating full agreement between  
307 labellers for all pixels, and 1 indicating complete disagreement.

### 308 2.2.2 Cropland classification model

309 Upon completing each batch of labels, the platform automatically launched a machine learning cluster  
310 (Elastic Map Reduce<sup>4</sup>) comprised of several hundred to a thousand CPUs, depending on the size of the  
311 AOI.

312 The first step in the process was to derive a set of features from the image composites. Previous work  
313 showed that a large number of simple features summarizing image reflectance and vegetation indices  
314 within local neighborhoods were highly effective for classifying smallholder croplands (Debats et al.  
315 2016). We followed that logic in this study, but used a smaller feature set because the storage and

---

<sup>4</sup><https://docs.aws.amazon.com/emr/latest/APIReference/emr-api.pdf>

316 memory required for our mapping geographies were several orders of magnitude larger. For each  
317 seasonal composite, we calculated the mean and standard deviation of each band within an 11X11 and  
318 5X5 moving window, respectively (initial tests revealed these two window sizes to be most effective).  
319 This provided an overall set of 24 features, including the unmodified bands of both composites (Table  
320 1).

321 Table 1. List of image features.

Feature	Window Size	N Features
RGB-NIR	1X1	8
Mean	11X11	8
Standard deviation	5X5	8

322 We used a combination of `GeoTrellis`<sup>5</sup>, `rasterio`<sup>6</sup>, and `RasterFrames`<sup>7</sup> to derive the features on the  
323 fly (which was enabled by converting the composites to Cloud-optimized Geotiffs<sup>8</sup>) and convert them  
324 into Apache Spark DataFrames.

325 The extracted features were combined with their corresponding training and validation labels and  
326 passed to the machine learning classifier, a `SparkMLlib` implementation of Random Forests (Breiman  
327 2001). We trained the model with a balanced sample and a tree depth of 15 and total tree number of  
328 60. Initial testing showed that model performance saturated with increasing values of these parameters  
329 (cluster failures occurred when tree depths and numbers were simultaneously  $\geq 16$  and  $\geq 50$ ,  
330 respectively), and that model stability was satisfactory with these settings, as there was  $\leq 0.01$   
331 difference in accuracy for separate models trained on the same labels.

### 332 2.2.3 Model performance

333 To assess performance of the Random Forests classifier, we used the validation sample to calculate  
334 binary accuracy, the F1 score (the geometric mean of precision and recall), and the area under the

---

<sup>5</sup><https://github.com/locationtech/geotrellis>

<sup>6</sup><https://rasterio.readthedocs.io/en/latest/>

<sup>7</sup><https://rasterframes.io/>

<sup>8</sup><https://www.cogeo.org/>

335 curve of the Receiver Operating Characteristic (Pontius and Si 2014), as well as the false positive rate.  
336 We calculated these measures each time the model was retrained for a given AOI, in order to assess the  
337 change in classifier performance with each active learning iteration.

338 To evaluate whether active learning improved model performance relative to randomized label selection,  
339 we ran an additional test within three AOIs (1, 8, and 15), in which we retrained the model with 100  
340 randomly selected labels for each iteration. We then compared the differences in accuracy, AUC, and  
341 F1 between the actively and randomly trained models (Debats et al. 2017).

342 To quantify the potential impact of label error on classification results, we conducted two further  
343 analyses. We evaluated the performance differences between models trained with three different sets of  
344 labels: 1) those from the lowest scoring labeller to map each training site, 2) those from the highest  
345 scoring labeller, and 3) the consensus labels. We also calculated the correlations between the mean  
346 Bayesian Risk of labels in each AOI and the corresponding model performance metrics (Table S3).

### 347 **2.3 Segmentation**

348 Upon completion of the active learning process, we deployed a five-step algorithm to create a  
349 segmented map of field boundaries (see Figure S3 for illustration of the steps). In the first step, we  
350 identified edge features within the imagery. To do this, we applied the meanshift algorithm (Yizong  
351 Cheng 1995) to each dry-season composite tile, and then passed a Sobel filter over the mean-shifted  
352 green, red, and near-infrared bands, and the corresponding map of predicted cropland probabilities. We  
353 then summed the four resulting edge images to produce a combined edge image.

354 In the second step, we used a compact watershed algorithm (Neubert and Protzel 2014) to segment the  
355 edge image, specifying a high number of segments (6,400) per tile, so that the mean segment size ( $<0.5$   
356 ha) was finer than the expected mean field size ( $>1$  ha).

357 In the third step, we hierarchically merged the resulting polygons. We first constructed a region  
358 adjacency graph for each tile, with each node representing all image pixels within each polygon. The  
359 edge between two adjacent regions (polygons) was calculated as the difference between the means of the  
360 normalized colors of all bands. We then merged the most similar pairs of adjacent nodes until there  
361 were no edges remaining below the predetermined threshold of 0.05.



362 In the fourth step, we overlaid the merged polygons with the cropland probability images, and polygons  
363 in which the mean probability was greater than 0.5 were retained as crop fields.

364 In the fifth and final step, we refined the crop field polygons, by removing holes and smoothing  
365 boundaries using the Visvalingam algorithm (Visvalingam and Whyatt 1993). We then merged  
366 neighboring polygons that overlapped along tile boundaries.

367 The resulting map represents dry season crop field boundaries, as we did not segment growing season  
368 images. We made this choice because labels were primarily drawn on dry season composites, when  
369 boundaries were typically more visible.

## 370 **2.4 Map assessment**

371 We followed recommended guidelines (Stehman and Foody 2019) to conduct an independent assessment  
372 of the categorical accuracy of the final maps, using a set of 1207 (487 cropland; 720 non-cropland)  
373 point-based, map reference labels, which were placed across Ghana using a stratified random sample  
374 design, and collected through the labelling platform by two expert supervisors (see SI for full details on  
375 sample design and collection). For efficiency, the supervisors labelled separate portions of the sample,  
376 but overlapped on a small subset ( $n = 23$ ). We calculated the label agreement (87%) on this subset to  
377 estimate uncertainty in the map reference sample (Stehman and Foody 2019). In addition to this, the  
378 sample was labelled with four classes: cropland; non-cropland; unsure but likely cropland; unsure but  
379 likely non-cropland. The last two classes, which constituted 15.7% of the sample, provided a further  
380 measure of uncertainty in the map reference sample

381 We used the sample to calculate the overall accuracy for each map, the class-wise User's and Producer's  
382 accuracy, and the 95% confidence intervals for each accuracy measure (Olofsson et al. 2013, Olofsson et  
383 al. 2014, Stehman and Foody 2019). We calculated these measures across the entire country, as well as  
384 several different zones, to evaluate regional difference in accuracy. We defined two sets of zonations  
385 (Figure S5), each containing four zones, the first created by grouping 1) the three northern AOIs (1-3),  
386 2) the six central AOIs (4-9), 3) the four southwestern AOIs (10, 11, 13, 14, 16), and 4) the two  
387 southeastern zones (13, 15). This grouping differs from the three clusters used to collect initial model  
388 training samples, as we designed these to divide the country more finely, and to isolate the less forested

389 southeastern third of Ghana from the more forest northwest. The second zonation was developed by  
390 grouping the country’s eight agro-ecological zones into four broader clusters (Figure S5B). We applied  
391 this zonation only to the per-pixel classification, to better understand patterns of error in the model.

392 To assess how effectively the segmentations captured field characteristics, we compared the size class  
393 distributions of the segmented field boundaries against those calculated from the field boundaries  
394 digitized by the labellers within the 100 validation sites from each AOI. We chose this approach  
395 because of existing uncertainties in polygon-based accuracy assessment methods (Ye et al. 2018), and  
396 because the map’s ability to represent field sizes was of greatest interest. To undertake this comparison,  
397 we selected the polygons from the most accurate labeller to digitize the 100 validation grids in each  
398 AOI, and calculated the average area and number of polygons in each cell. We then calculated the  
399 same statistics from the segmented boundaries that intersected each validation grid, and compared the  
400 two sets of statistics.

401 We used the final maps to evaluate the characteristics of Ghana’s croplands. We calculated the  
402 estimated area of cropland in Ghana, as well as the average size and total number of fields in the  
403 different AOIs. We used the map reference sample to calculate adjusted area estimates and confidence  
404 intervals for each map class, and used the differences between labellers’ polygons and segmented  
405 boundaries at validation sites to calculate bias-adjusted estimates of mean field sizes and the total  
406 number of fields.

## 407 **3 Results**

408 Our results produced two separate maps of Ghana’s annual croplands, over a total area of 248,343 km<sup>2</sup>  
409 that included portions of the neighboring countries overlapped by image tiles.

### 410 **3.1 Image quality**

411 The assessment of image composites found that their quality in both seasons was highest in the  
412 northern half of the country and lowest in the southwest, (Figure 3A), where the substantially greater  
413 cloud cover resulted in a much lower density of available PlanetScope imagery for each time period  
414 (Figure S6). The average quality score of growing season composites was 0.88, with 70 percent having

415 scores  $\geq 0.85$  (out of 1; Figure 3B), while the mean score of dry season composites was 0.92 (74 percent  
416  $\geq 0.85$ ).

## 417 **3.2 Cropland probabilities**

418 To make the initial maps of cropland probabilities, the active learning process ran for 3 iterations in 12  
419 of 16 AOIs, varying from as little as 1 to as many as 4 iterations across the other 4 AOIs, with the  
420 number of iterations varying according to the performance of the starter models (i.e. AOIs with higher  
421 starting performance stopped after fewer iterations, see SI). Each AOI's model was trained by 300-500  
422 randomly selected labels (Figure S7A), plus an additional 600 - 900 (typically 800) labels within each  
423 AOI that were selected by active learning. Actively selected labels showed distinctive patterns in  
424 several AOIs (Figure S7B), such as concentrating along ecotones or the boundaries of agro-ecological  
425 zones. A total of 6,299 training and 1,600 validation labels were collected by 20 labellers to develop and  
426 assess model performance (Figure S8).

### 427 **3.2.1 Performance gains during active learning**

428 The performance of the Random Forest classifier typically improved with each active learning iteration.  
429 The average accuracy, AUC, and F1 at iteration 0 were 0.786, 0.809, and 0.464, respectively, increasing  
430 to 0.825, 0.818, and 0.507 by iteration 3 (Figure 4). These differences represent respective gains of 4.9,  
431 1.1, and 9.1 percent for the three metrics. The largest gains for each metric occurred on iteration 1,  
432 averaging 2.9, 1, and 3.8 percent for accuracy, AUC, and F1, while the lowest gains were realized on  
433 iteration 3, with accuracy, F1, and AUC respectively increasing by just 1.2%, 0.9%, and 0.3%. The  
434 scores achieved on the final iteration varied substantially across AOIs and metrics. Accuracy ranged  
435 between 0.725 (AOI 15) and 0.948 (AOI 16), while AUC varied from 0.725 (AOI 4) and 0.93 (AOI 11),  
436 and F1 from 0.252 (AOI 13) and 0.636 (AOI 8).

437 The experiment conducted in three AOIs (in AOIs 1, 8, and 15) showed that training models with  
438 active learning improved performance compared to randomized approaches to label selection. After  
439 three iterations, the accuracy, AUC, and F1 scores for the actively trained models were respectively 0.8,  
440 0.6, and 2.3 percent higher than those for randomly trained models (Figure S9). However, there was  
441 more variability in earlier iterations, with average score differences of -1.7 (accuracy), 0.6 (AUC), and

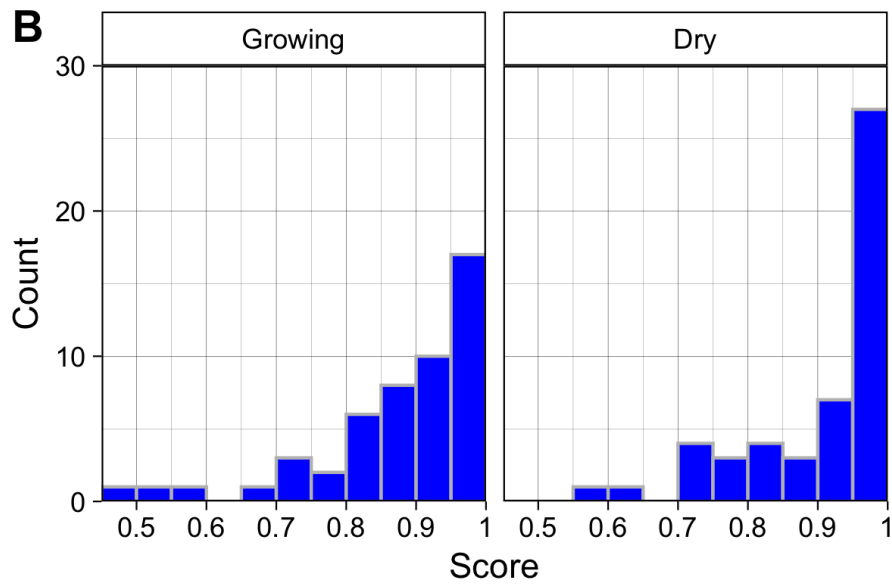
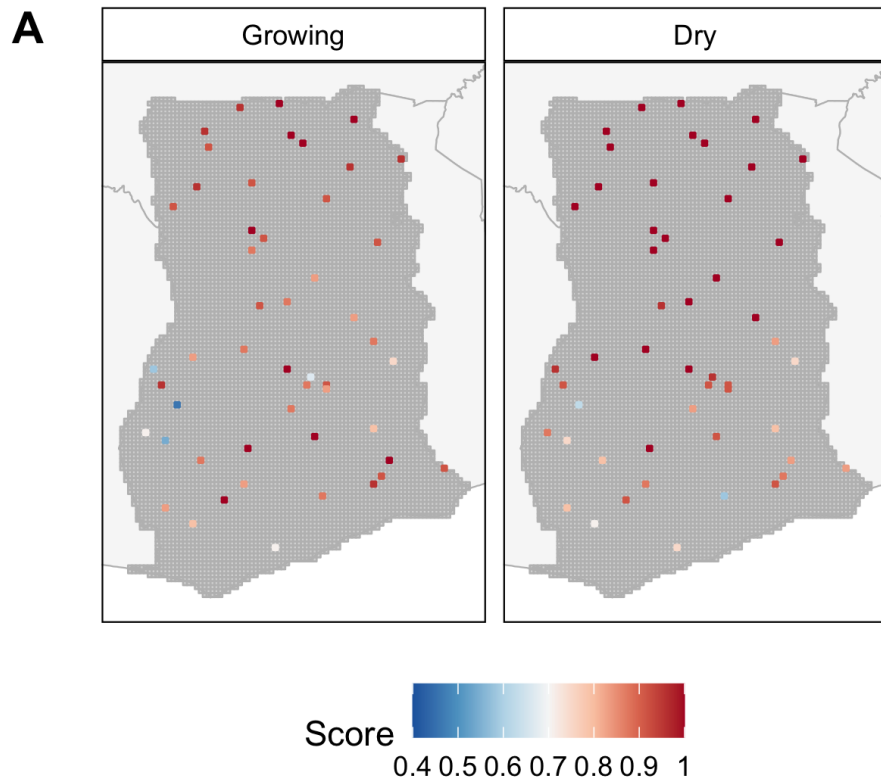


Figure 3: The location and quality scores of 100 randomly selected tiles for the growing (A) and off-growing season (B), and the corresponding distributions of the quality scores for each season, respectively (C and D).

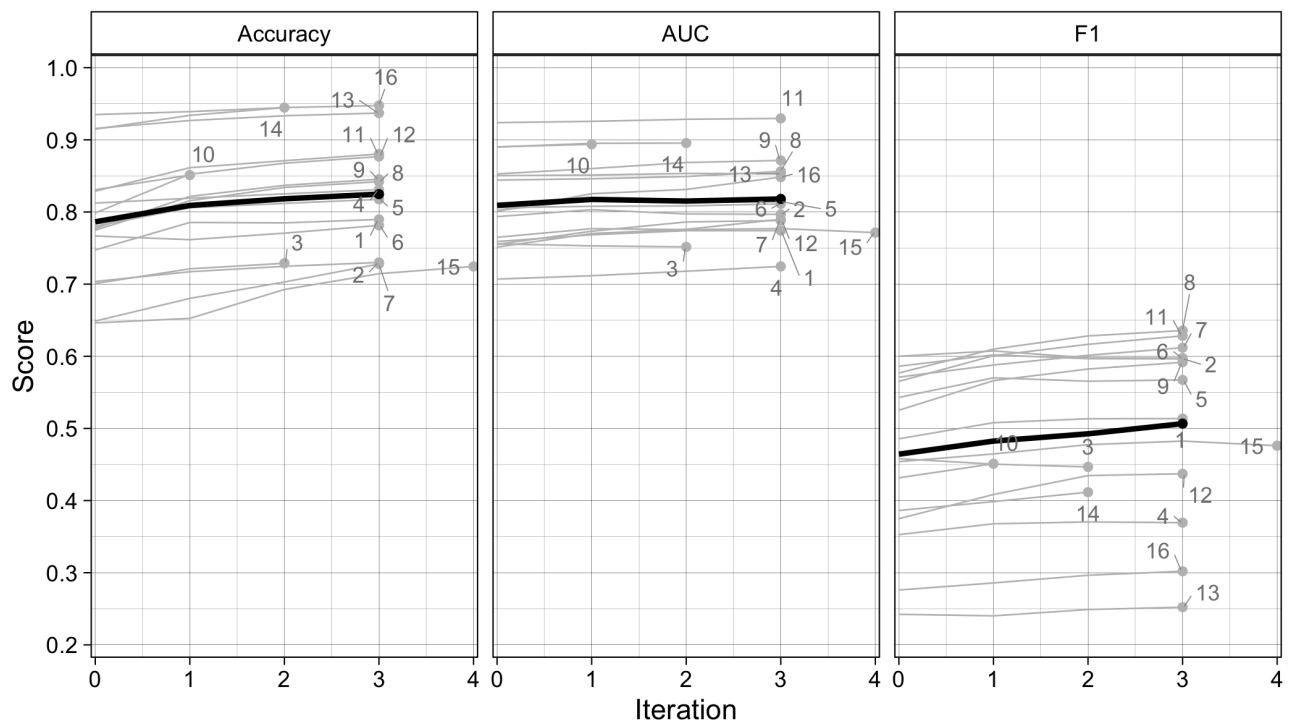


Figure 4: Scores for overall accuracy, area under the curve of the Receiver Operating Characteristic, and the F1 scores for the Random Forests model results after each iteration of the active learning loop for each AOI (gray lines), as well as the mean score per iteration across all AOIs (black lines).

442 0.8 percent (F1) after iteration 1, and -0.3 (accuracy), 0.4 (AUC), and 1.8 (F1) percent after iteration 2  
443 (see SI for more details).

### 444 **3.2.2 The impact of label error and uncertainty on model performance**

445 We used the two measures of label quality calculated by the platform, the average quality score of each  
446 labeller and Bayesian Risk (or simply “label risk”), to assess the potential impacts of label error on  
447 model performance. The average of each labeller’s AOI-specific accuracy score was 0.71 (range 0.6 to  
448 0.85; see Figures S7 and S8 for details on label scores and number of assignments per labeller). The  
449 average Bayesian Risk was 0.124, with highest label risk (0.165) in the northern AOIs (AOIs 1-6;  
450 Figures S10-11), lowest (0.165) in the southwestern AOIs (AOIs 10, 11, 13, 14, 16), and intermediate  
451 (0.131) in the central-southeastern AOIs (AOIs 7-9, 12, 15).

452 Treating each labeller’s average label quality scores (Figure S10) as a proxy for error, we used these  
453 scores to develop training sets to test the impact of label error on model performance. The results of  
454 these tests, which were conducted in AOIs 1, 2, 8, and 15, showed that the average accuracy, AUC, and  
455 F1 scores for models trained with the consensus labels were respectively 0.772, 0.8, and 0.555 (Figure  
456 5). Performance metrics from consensus-trained models were just 0.5 - 1.2 percent higher than those  
457 models trained with the most accurate individuals’ labels (accuracy = 0.762; AUC = 0.796; F1 = 0.55),  
458 but were 11.6 - 27.4 higher than models trained with the least accurate individual labels (accuracy =  
459 0.606; AUC = 0.716; F1 = 0.44).

460 Correlations (Table S3) between the mean label risk per AOI (Figures S11-12) and model performance  
461 metrics showed strong (Spearman’s Rank Correlation = -0.824) to moderate ( $r = -0.568$ ) negative  
462 correlations between label risk and accuracy and AUC, respectively, while F1 had a weaker but  
463 moderate positive association ( $r = 0.456$ ). The positive sign of the latter relationship is  
464 counter-intuitive, but is explained by risk’s association with precision, one of two inputs to F1, which  
465 was moderately positive ( $r = 0.629$ ), whereas risk had a negligible correlation with recall ( $r = 0.206$ ),  
466 F1’s other component. The correlation between risk and the false positive rate ( $r = 0.688$ ), another  
467 important performance metric, shows that labelling uncertainty may increase model commission error.

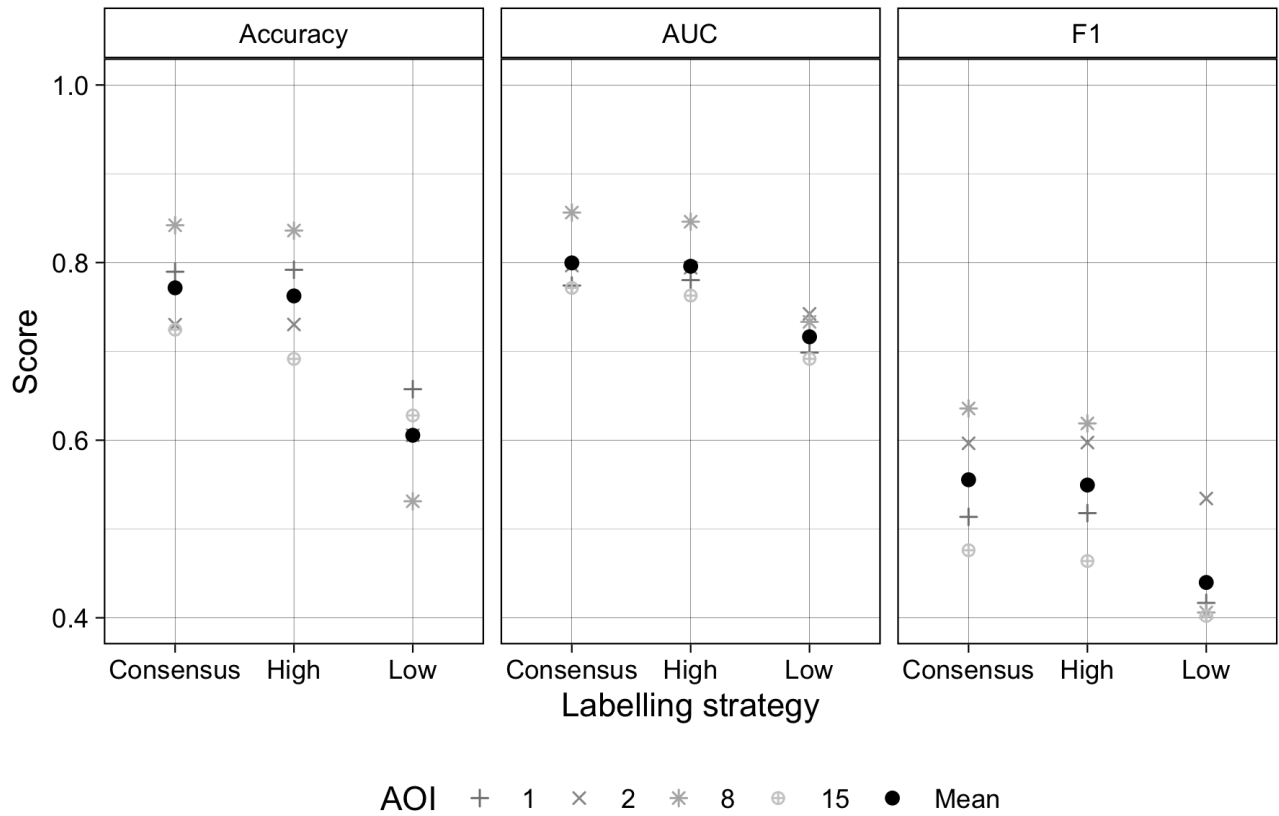


Figure 5: Scores for overall accuracy, area under the curve of the Receiver Operating Characteristic, and the F1 score resulting from models trained with consensus labels, and labels made by the most and least accurate labellers to map each site. Comparisons were made for AOIs 1, 2, 8, and 15, denoted by grey symbols, while the mean scores across these AOIs are shown for each metric.

### 468 **3.3 Map accuracy**

#### 469 **3.3.1 Categorical accuracy**

470 We used the map reference sample to evaluate the accuracy of the cropland probability map (after  
471 classifying it using a threshold probability of 0.5) and the map of segmented field boundary maps. We  
472 found that the overall accuracy of the pixel-wise classifications was 88% against this map reference  
473 sample (Table 2). Confining the map reference sample to four distinct zones (Figure S4A) shows that  
474 overall accuracy ranged from 83.3% in Zone 1 (AOIs 1-3) to 93.6% in Zone 3 (AOIs 10, 11, 13, 15, and  
475 16). The Producer's accuracy of the cropland class was 61.7% across Ghana, ranging from 45.6% in  
476 Zone 3 to 67.9% in Zone 1, while the User's accuracy was 67.3% overall, ranging from 59.8% in Zone 4  
477 to 71.2% in Zone 1. Both measures of accuracy were substantially higher for the non-cropland class  
478 across all zones, typically exceeding 90%. The lowest accuracies for the non-cropland class was in Zone  
479 1 (Producer's = 89.3%; User's = 87.7%).

480 The overall accuracies obtained from the segmented maps were generally 1-2 percentage points lower  
481 than those of the per-pixel maps, while User's accuracies tended to be 8-10 percentage points less  
482 (Table 2). In contrast, Producer's accuracies were 15-20 points higher than in the per-pixel map. The  
483 segmentation step therefore helped to reduce omission error while substantially increasing commission  
484 error.

#### 485 **3.3.2 Segmentation quality**

486 The comparisons of digitized versus segmented field boundaries showed that the mean field size across  
487 all validation sites averaged 4.97 ha (Median = 3.75; StDev = 6.04), which was 1.41 times larger than  
488 the 2.06 ha (Median = 1.35; StDev = 3.26) mean area of labeller-digitized polygons. This discrepancy  
489 was primarily caused by results in four AOIs (2, 3, 7, and 15; Figure S14), where segments averaged  
490 between 7.76 and 10.76 ha, compared to 2.18 - 2.77 ha for the corresponding hand-digitized polygons.  
491 The number of segmented fields per validation site averaged 3.08 (median = 2.66; StDev = 2.9)  
492 compared to 4.4 (median = 3.38; StDev = 4.52) for digitized polygons (Figure S15).



Table 2: Map accuracies and adjusted area estimates for the 3 m pixel-wise classifications (based on Random Forests predictions; top 5 rows) and the segmented map (bottom 5 rows). Results are provided for 4 zones (Zone 1 = AOIs 1-3; Zone 2 = AOIs 4-9; Zone 3 = AOIs 10, 11, 13, 14, 16; Zone 4 = AOIs 12, 15) plus the entire country. The error matrix (with reference values in columns) provides the areal percentage for each cell, and the Producer's (P), User's (U), and overall (O) map accuracies and their margins of error (in parenthesis) are provided, as well as the sample-adjusted area estimates (in km<sup>2</sup>) and margins of error.

		Non-crop	Crop	Total	U	O	n	Area	
Per-pixel classification	Zone 1	Non-crop	64.2	9	73.2	87.7 (5.5)	83.3 (4.3)	138	40992 (2468)
		Crop	7.7	19.1	26.8	71.2 (5.9)		226	16025 (2468)
		P	89.3 (5.5)	67.9 (5.9)					
		n	186	178					
	Zone 2	Non-crop	73.9	6.7	80.6	91.7 (4.2)	86.5 (3.6)	169	65123 (2866)
		Crop	6.8	12.6	19.4	64.8 (6.0)		247	15533 (2866)
		P	91.5 (4.2)	65.3 (6.0)					
		n	242	174					
	Zone 3	Non-crop	89.6	4.8	94.4	94.9 (3.2)	93.6 (3.1)	177	70885 (2413)
		Crop	1.6	4	5.6	71.4 (9.0)		98	6860 (2413)
		P	98.2 (3.2)	45.6 (9.0)					
		n	196	79					
	Zone 4	Non-crop	80.7	5.3	85.9	93.8 (5.9)	89.1 (5.3)	65	26473 (1615)
		Crop	5.7	8.4	14.1	59.8 (10.4)		87	4199 (1615)
		P	93.4 (5.9)	61.4 (10.4)					
		n	96	56					
	Ghana	Non-crop	77.2	6.7	83.9	92.0 (2.3)	88.0 (2.0)	549	202856 (4904)
		Crop	5.3	10.8	16.1	67.3 (3.6)		658	43233 (4904)
		P	93.6 (2.3)	61.7 (3.6)					
		n	720	487					
Segmentation	Zone 1	Non-crop	57.6	4.2	61.8	93.2 (5.3)	81.4 (3.9)	88	40890 (2236)
		Crop	14.4	23.8	38.2	62.3 (5.7)		276	15905 (2236)
		P	80.0 (5.3)	84.9 (5.7)					
		n	186	178					
	Zone 2	Non-crop	70.4	3.7	74.1	95.0 (3.9)	85.2 (3.2)	121	65642 (2599)
		Crop	11.2	14.8	25.9	56.9 (5.7)		295	14841 (2599)
		P	86.3 (3.9)	80.1 (5.7)					
		n	242	174					
	Zone 3	Non-crop	86.6	3	89.6	96.6 (2.9)	92.6 (2.8)	148	71695 (2181)
		Crop	4.3	6.1	10.4	58.3 (8.6)		127	7167 (2181)
		P	95.2 (2.9)	66.7 (8.6)					
		n	196	79					
	Zone 4	Non-crop	75.3	3.4	78.7	95.7 (6.0)	86.1 (5.1)	46	26712 (1593)
		Crop	10.4	10.8	21.3	50.9 (9.6)		106	4446 (1593)
		P	87.8 (6.0)	76.0 (9.6)					
		n	96	56					
	Ghana	Non-crop	73.2	3.6	76.8	95.3 (2.1)	86.7 (1.8)	403	204940 (4395)
		Crop	9.7	13.5	23.2	58.2 (3.4)		804	42359 (4395)
		P	88.3 (2.1)	78.9 (3.4)					
		n	720	487					

### 493 3.4 Ghana's croplands

494 Two separate maps of cropland were produced for each AOI, a per-pixel map derived from the cropland  
495 probabilities, and the vectorized map of field boundaries (Figure 6). The former provides the more  
496 accurate picture of cropland distributions in Ghana, which are most concentrated in the Southeastern  
497 corner (AOI 15), the central-western region (AOI 7, the northeastern and northwestern corners of AOIs  
498 10 and 11, and the south of AOI 8), and the northeastern quadrant stretching from AOI 9 through AOIs  
499 5 and 6 and up to AOIs 2 and 3. The northern third of AOI 1 also has noticeable densities of cropland.  
500 Several prominent areas of low cropland density indicate the presence of large protected areas, such as  
501 Mole National Park in the southeastern corner of AOI 1 and Digya National Park in the northwestern  
502 corner of AOI 12. The relative absence of cropland in AOIs 13, 14, and 16 does not reflect the scarcity  
503 of agriculture in these areas, but rather the predominance of tree crops, which we did not map.

504 Using the map reference sample and each map, we made two separate estimates of the total cropland  
505 area in Ghana in 2018. The cropland extent estimated from the field boundary map was 42,359 km<sup>2</sup>  
506 (with a margin of error of 4,395 km<sup>2</sup>), or 17.1% (15.4-18.9%) of the mapped area. The estimate from  
507 the per pixel map was 43,233 km<sup>2</sup> (margin of error = 4,904 km<sup>2</sup>), or 17.6% (15.6-19.6%) of area.

508 The field boundary map provides additional information on how the characteristics of croplands vary  
509 across Ghana, ranging from narrow, strip-like fields in parts of AOI 15 (Figure 6's lower right inset) to  
510 more densely packed, less distinctly shaped fields in AOI 5 (upper right inset in Figure 6). To explore  
511 how field characteristics varied geographically, we mapped the average size and total number of fields  
512 within each 0.05 degree tile grid (Figure S16). These patterns generally correspond to those seen in the  
513 cropland density map (Figure 6), with larger sizes and field counts occurring where field densities were  
514 higher, although the biases (relative to the validation labels) in both measures (Figures S14-15)  
515 complicate interpretations of those variations. To minimize this complication, we used the calculated  
516 biases to develop adjusted estimates of field size and count (Table 3). These adjusted estimates show  
517 that the typical field size in Ghana is 1.73 ha, ranging from 0.96 in AOI 4 to 2.82 ha in AOI 4, with  
518 fields in the forest zone AOIs (10, 11, 13, 14, 16) generally smaller than those in the northern half of  
519 the country (Table 3). The estimated total number of fields is 1,662,281, or 205 fields per tile grid cells,  
520 varying from 108 fields/tile cell in AOI 4 to 399 in AOI 6.

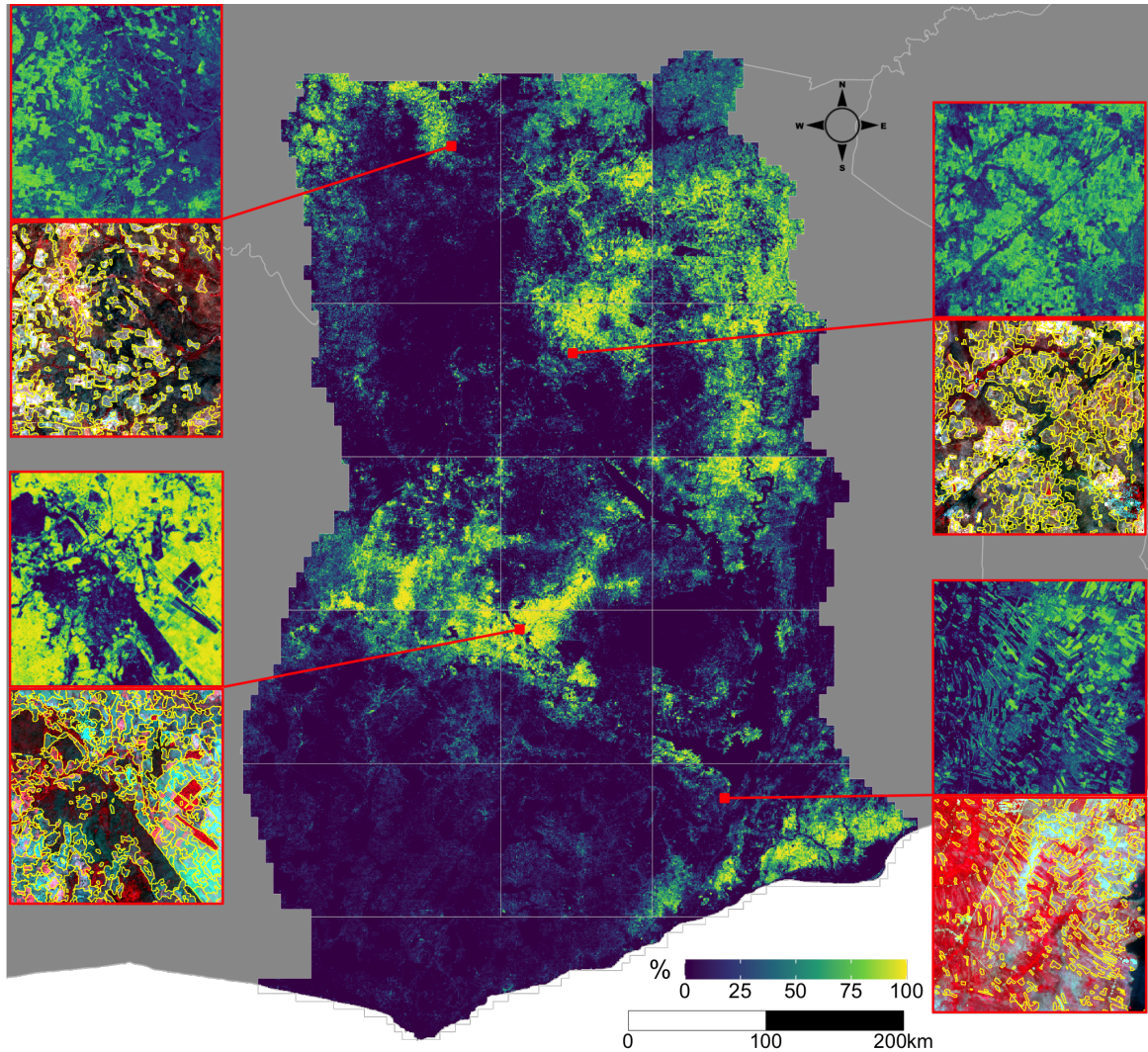


Figure 6: The distribution of croplands in Ghana. The main map shows the percentage of croplands in each 0.005 degree grid cell, derived from the predicted cropland probabilities. The insets on the margins illustrate predicted probabilities (top map in each couplet) at original image resolution (0.000025 degrees) and segmented field boundaries overlaid on the dry season PlanetScope composite, for four separate tiles. Each tile's position is shown on the main map, and is color-coded to the boundary lines around its corresponding inset.

Table 3: The average size and total number of crop fields for each AOI and for Ghana overall. The original and bias-adjusted values for each measure are provided, as well as the total number of 0.05° degree tiles in each AOI.

AOI	N tiles	Size	Size (adj)	N	N / tile	N (adj)	N (adj) / tile
1	777	3.71	1.26	97,822	126	127,580	164
2	597	7.66	1.96	87,666	147	120,651	202
3	501	8.24	2.18	108,819	217	104,422	208
4	465	2.44	2.82	26,276	57	50,163	108
5	400	4.24	2.09	43,290	108	53,756	134
6	429	5.10	2.15	81,363	190	145,347	339
7	471	5.64	1.49	93,282	198	123,005	261
8	400	4.89	1.98	55,500	139	78,868	197
9	479	4.10	1.82	72,081	150	89,840	188
10	630	2.24	1.04	119,019	189	170,907	271
11	400	3.65	1.52	52,510	131	94,709	237
12	471	3.44	1.77	44,667	95	52,947	112
13	627	0.84	0.96	67,996	108	125,368	200
14	400	1.09	2.72	56,006	140	101,767	254
15	548	4.95	1.54	75,752	138	105,681	193
16	521	0.95	1.41	49,097	94	117,268	225
Ghana	8,116	3.92	1.73	1,131,146	139	1,662,281	205

## 521 4 Discussion

522 These results demonstrate a capability to map the characteristics of smallholder-dominated cropping  
523 systems at high spatial resolution, annual time steps, and national scales. The resulting maps provide  
524 an updated and more granular view of the distribution and extent of croplands in Ghana,  
525 complementing existing national to regional land cover maps derived from moderate resolution imagery  
526 (Hackman et al. 2017, Xiong et al. 2017, ESA n.d.). Those prior studies estimated that cropland covers  
527 19.4 (Xiong et al. 2017) to 32% (Hackman et al. 2017) of Ghana in 2015. In contrast, our 2018 maps  
528 provide a raw estimate of 16.1-23.2% cover (Table 2), and our map reference sample-based estimate was  
529 17.1-17.6%. Our results thus suggest that Ghana’s croplands are less extensive than those previous  
530 estimates. However, this difference may arise from our use of a cropland definition that excludes longer  
531 fallows and abandoned fields, which in some regions may comprise over half of total cropland area  
532 (Tong et al. 2020).

533 In addition to this updated information on Ghana’s cropland extent and distribution, our results

534 provide new insights into field size and number at a national scale (Figures 6, S11-12). Previous efforts  
535 to map smallholder field boundaries have either used *in situ* data collection (Carletto et al. 2013, 2015)  
536 or remote sensing studies over relatively small (e.g. Forkuor et al. 2014, Persello et al. 2019) or  
537 discontinuous (Estes et al. 2016a) areas. The most extensive studies to date enlisted crowdsourced  
538 volunteers to classify fields visible within high resolution imagery sampled from virtual globes into  
539 broad size categories (Fritz et al. 2015, Lesiv et al. 2019). Those efforts included country-specific  
540 results for Ghana ( $n = 263$ ), which yield an average field size estimate of 5.33 ha<sup>9</sup>. This estimate  
541 exceeds our Ghana-wide average segment size (3.92 ha; Table 3), but is closer to the mean (4.97 ha)  
542 within AOIs 1-9, 12, and 15, which is where most of the crowdsourced sample appears to have been  
543 collected. However, our bias-adjusted estimates of 1.73 (Ghana-wide) and 1.87 (AOIs 1-9, 12, and 15)  
544 ha were much smaller.

#### 545 4.1 Map accuracy and key sources of error

546 Although these maps provide valuable new information, they nevertheless contain substantial errors  
547 that can impact “downstream” uses (e.g. estimating crop production estimates) and decisions based on  
548 these maps in unpredictable ways (Estes et al. 2018). The overall accuracies (86.7-88%, Table 2) are  
549 near the boundary of what might be considered *achievable* map accuracy (Elmes et al. 2020), given  
550 that we only have ~85% confidence in our map reference sample, which is our best estimate of the  
551 “truth.” However, accuracies for the cropland class were much lower, falling between 62 (producer’s)  
552 67 (user’s) percent country-wide for the per-pixel map (Table 2), meaning the model produced  
553 substantial commission and omission errors for this class. The segmented boundary maps had fewer  
554 omission errors (producer’s accuracy = 79%), but higher false positives (user’s accuracy = 58.2%).  
555 These accuracies are near the middle to upper ranges of those reported for the cropland class in other  
556 large-area mapping studies (Hackman et al. 2017, Xiong et al. 2017, Lesiv et al. 2017).

557 The patterns of accuracies within the cropland class varied by zone. These zones largely align, albeit  
558 with some discrepancies, with the country’s agro-ecological zones (AEZs), thus the accuracy patterns  
559 may be in part because some regions are simply more difficult to map. Producer’s accuracy for both

---

<sup>9</sup>Obtained by calculating the weighted mean from the count of the five size classes and the mean of the hectare range provided for the four smallest size classes, and the lower bound of the size range provided for the largest size class. Data sourced from Table S3 in Lesiv et al. 2019.

560 maps was highest in the two northern zones (1 and 2), which are primarily savannas (Figure S4), and  
561 lowest in zones 3 and 4, which are comprised of forest or coastal savannas. User’s accuracy followed a  
562 similar pattern, with the exception of Zone 3, which had the highest user’s accuracy, albeit from a very  
563 small sample. Aligning the reference samples more precisely with agroecozone boundaries (Figure S4B)  
564 provides further insight into error patterns within the per-pixel map’s cropland class (Table S4).  
565 Coastal savannas in the southeast had the highest producer’s and lowest user’s accuracy, perhaps  
566 because this region has high density cropland inter-mixed with uncultivated areas that have low woody  
567 cover, which could help promote commission error. Maps in the northern savannas had the best  
568 balance between omission and commission error, and had the highest overall user’s accuracy. The  
569 transitional zone between forest and savanna had a very low Producer’s accuracy (21%), which likely  
570 reflects the fact that it was divided between several AOIs for mapping (Figure S4), and thus was  
571 under-represented in the training samples, particularly in AOIs 10 and 11 (Figure S7B).

572 Beyond the errors linked to regional differences, several other important factors contributed to map  
573 error. The first of these related to the mapping extent and image resolution. Given the goal of  
574 developing a high resolution, country-scale map, the large data volume constrained us to use a  
575 relatively small feature set and less than the recommended tree number and depth (Maxwell et al.  
576 2018) in our Random Forests models, in order to limit computational costs. Previous work found that  
577 Random Forests achieves much better performance on small-scale croplands when trained on a much  
578 larger number of features (Debats et al. 2016, Lebourgeois et al. 2017). However, applying such a large  
579 feature set within the extent of our AOIs was not possible, as the computing time and costs would have  
580 been several times larger<sup>10</sup>. This reduced the skill of the model, particularly when it came to  
581 differentiating cropland from bare or sparsely vegetated patches, which were common in many AOIs.

582 The inherent difficulty of the labelling task was another major limiting factor. Our platform was  
583 designed to minimize label errors, but determining croplands from non-croplands in these agricultural  
584 systems can be difficult. Labellers had to evaluate multiple image sources and to rely heavily on their  
585 judgment, which inevitably led to errors. Interpretation was particularly hard where croplands and  
586 surrounding landscapes had similar dry season reflectances, which was a particular problem in the  
587 northernmost savannas. Smaller field sizes also complicated labelling, as these become increasingly

---

<sup>10</sup>Each active learning iteration ran for ~4-8 hours on 800 CPUs, followed by a final ~10-14 hours for prediction

588 indistinct in the  $\sim 4$  m PlanetScope composites. The difficulty of labelling is reflected in the magnitude  
589 of the Bayesian Risk metrics (Figures S11-12), and by the average assignment quality scores of each  
590 labeller (71%; Figure S10). Although prior work (Rodríguez-Galiano et al. 2012, Mellor et al. 2015)  
591 found that Random Forests are robust to label error, we found that it has substantial impact (Figure  
592 5), which suggests that improving label quality is one of the most important factors in increasing model  
593 accuracy. Newer models, such as convolutional neural networks, may be less sensitive to label error,  
594 provided the error is random and the map reference samples are of high quality (Burke et al. 2021).  
595 However, over many smallholder systems training label errors will likely be biased in a particular  
596 direction (e.g. towards omission when fields are not easily distinguished from the background), and our  
597 results show that reference labels can have substantial uncertainty.

598 Image quality was another issue, although primarily in the forested AOIs, where frequent cloud cover  
599 and the corresponding lower number of available images resulted in lower quality composites (Figure 3),  
600 with more brightness artifacts and blur. This impacted labellers' abilities to discern fields, and  
601 doubtless affected model predictions. Little can be done to mitigate these errors, short of confining  
602 imagery to the less cloudy dry season, which could reduce model performance by removing the temporal  
603 contrast (Debats et al. 2016, Defourny et al. 2019), or by adding radar data (e.g. Sentinel-1) to the  
604 predictor set, which would reduce map resolution. Composite quality could be improved by using  
605 imagery from the same seasons over multiple years, but this would undermine the goal of developing  
606 annual maps, while the dynamism of the croplands would blur field boundaries within the imagery.

607 The final major source of error arose from the segmentation process. The vectorized maps had high  
608 commission errors caused by uncertainties in the Random Forests predictions. Model uncertainty meant  
609 that many pixels in non-cropland areas had probabilities with values near 0.5. Segments in these areas  
610 were retained if the average probability of intersected pixels exceeded the 0.5 classification threshold. A  
611 more accurate classifier would reduce such errors, as would a locally varying classification threshold (e.g.  
612 Waldner and Diakogiannis 2020). Over-merging was another source of error in the segmentation  
613 algorithm, which led to overestimated field sizes and unrealistic shapes in some areas, particularly in  
614 high density croplands (e.g. in AOIs 2 and 8; Figure 6) where boundaries between adjacent fields were  
615 indistinct in the imagery. Preventing merging could help in such cases, but potentially lead to  
616 over-segmentation, thereby underestimating field sizes.

## 617 4.2 Error mitigation features

618 Despite these numerous sources of errors, our approach was effective in mitigating several of these error  
619 sources. Label quality assessment and consensus labelling were the most effective error mitigation tools.  
620 Label quality scores allowed us to quantify the impact of label error on model performance (Figure 5),  
621 while consensus labels produced maps that were more accurate than they would have been if we had  
622 relied on individually generated labels. The quality scores also helped to improve the overall accuracy  
623 of consensus labels, by placing higher weight on the work of more accurate labellers. In addition to  
624 these benefits, label quality scores (Figure S10) also allowed us to select the labels most likely to  
625 accurately capture field sizes and numbers, which we used to estimate and correct the biases in these  
626 two measures derived from the segmented field boundaries.

627 Active learning improved overall model performance relative to randomized training site selection, in  
628 line with findings from two recent efforts (Debats et al. 2017, Hamrouni et al. 2021). Although the  
629 relative performance gains that we observed were smaller (e.g. Debats et al. (2017) 29% higher model  
630 performance after one iteration, and 8% higher on the final iterations), those comparisons were made  
631 by starting with a training sample that was  $<1/10$  the size of ours. Our large starter sample meant  
632 that the models were substantially trained before they were exposed to actively selected labels, thereby  
633 diluting their impact on performance. Nevertheless, we found higher performance from active learning,  
634 most notably in the F1 score (Figure S9), a balanced performance metric, which further demonstrates  
635 its effectiveness.

636 The detail, temporal precision, and large extent of our maps was enabled by our use of PlanetScope  
637 data, which is currently the only source of sub-5 meter imagery with daily coverage (McCabe et al.  
638 2017). These spatial-temporal characteristics, together with the compositing technique we developed,  
639 allowed us to develop a complete image catalog for Ghana covering the two major seasons in the 2018  
640 agricultural year. Daily revisits were key to this capability, as they increased the number of cloud-free  
641 observations that could be collected in each season. Over rainy tropical regions, such as southern  
642 Ghana, the odds of obtaining a single clear PlanetScope observation within a 1-2 week period is often  
643 less than 50% (Roy et al. 2021). Although Sentinel-2 is free and has sufficient spatial resolution to  
644 effectively classify small-scale croplands (e.g. Defourny et al. 2019, Kerner et al. 2020), its 5-day



645 interval is likely too infrequent to generate adequate seasonal composites over much of Ghana. The  
646 smaller number of clear observations that Sentinel-2 can provide compared to a daily acquisition  
647 schedule would result in greater reflectance discontinuities and residual cloud cover in the resulting  
648 composites. Given Ghana’s persistent cloudiness, such artifacts were present in a number of our  
649 PlanetScope composites. However, these were not large enough to have an appreciable impact on the  
650 resulting maps, as the mapping algorithms appeared to be relatively insensitive to these anomalies and  
651 any discontinuities along tile boundaries.

### 652 **4.3 Lingerin** questions

653 Several potential issues not addressed in our assessment merit further exploration. One of these was the  
654 degree of correspondence between image- and ground-collected labels. However, such comparisons may  
655 reveal unresolvable discrepancies between the two perspectives. The highly dynamic nature of these  
656 agricultural systems means that relatively narrow differences between the dates of ground- and  
657 image-based label collection can lead to substantial disagreement, simply because the fields themselves  
658 may have shifted during the interval (Elmes et al. 2020). These discrepancies can be exacerbated by  
659 the definition used to determine what constitutes a field, which might vary on the ground depending on  
660 who is being asked, or who is doing the collecting. These factors suggest that difference between  
661 ground- and image-collected labels would not necessarily indicate how far image labellers were from the  
662 “truth.” Nevertheless, a comparison against ground data would help to assess how accurately  
663 image-collected labels capture the typical size of fields, and thus merits further investigation.

664 The temporal discrepancies mentioned above (and discussed in Elmes et al. 2020) are another reason  
665 why we chose not to label on basemap imagery (in addition to restrictive usage terms), which is  
666 typically several years old (Lesiv et al. 2018). However, we did not assess whether the higher label  
667 accuracy one might achieve by digitizing on a <1-2 m resolution basemap would offset model errors  
668 caused by temporal mismatches.

669 Another potential issue is the degree to which our assessment of label error on model performance  
670 (Figure 5) was influenced by the validation dataset we used, which was based on consensus labels. This  
671 could have confounded the analysis, particularly when comparing the consensus label-trained models  
672 with those trained with the most accurate individual labels. However, a visual assessment of the

673 resulting probability maps confirms that models trained with the consensus and most accurate  
674 individual labels were more precise than the model trained with lower quality labels (Figure S13).

#### 675 **4.4 Broader applications**

676 This work demonstrates a proof of concept for developing high resolution, annual maps of  
677 smallholder-dominated croplands at national to regional scales, using an approach that follows  
678 recommended best practices for training and assessing machine learning models (Elmes et al. 2020).  
679 This approach can be readily updated to integrate improvements, such as newer machine learning  
680 models. Beyond providing valuable insights into field characteristics, field boundary maps can help  
681 improve remote estimation of crop areas and yield (e.g. Estes et al. 2013), and provide deeper insights  
682 into important socioeconomic aspects of agricultural systems, such as the relationships between  
683 agricultural productivity and farm size (Feder 1985, Carletto et al. 2013, Desiere and Jolliffe 2018).  
684 Such maps will be important for understanding the rapid agricultural change that is currently  
685 occurring in Africa.

#### 686 **4.5 Data availability and usage**

687 The maps presented here are a version 1 product that is freely available to use, along with its  
688 underlying code (see SI). In their current form, they may be useful for a variety of research applications.  
689 For example, analyzing the distributions of values in the probability maps may provide additional  
690 insight into the relative extents of active versus fallow croplands (Tong et al. 2020). However, use of  
691 these data for inventory estimates, to develop other map products, or to guide decision-making should  
692 be made with caution and account for the reported errors (Olofsson et al. 2014, Estes et al. 2018,  
693 Stehman and Foody 2019).

### 694 **5 Acknowledgements**

695 The primary support for this work was provided by Omidyar Network’s Property Rights Initiative, now  
696 PLACE. Additional support was provided by NASA (80NSSC18K0158), the National Science  
697 Foundation (SES-1801251; SES-1832393), and Princeton University. Computing support was provided  
698 by the AWS Cloud Credits for Research program and the Amazon Sustainability Data Initiative.

699 Azavea provided significant contributions in engineering the machine learning pipeline. We thank  
700 Meridia for providing information about local cropping systems and the characteristics of fields, and  
701 Radiant Earth Foundation for advice and guidance regarding machine learning best practices. We  
702 thank Manushi Trivedi, Sitian Xiong, and Tammy Woodard for their contributions to the underlying  
703 datasets and methods, and Michelle Gathigi, Omar Shehe, and Primoz Kovacic for support and  
704 management of the labelling efforts.

## 705 **6 References**

- 706 Azavea. 2020. Raster Foundry. <https://github.com/raster-foundry/raster-foundry>.
- 707 Bey, A., A. Sánchez-Paus Díaz, D. Maniatis, G. Marchi, D. Mollicone, S. Ricci, J.-F. Bastin, R. Moore,  
708 S. Federici, M. Rezende, C. Patriarca, R. Turia, G. Gamoga, H. Abe, E. Kaidong, and G. Miceli.  
709 2016. Collect Earth: Land Use and Land Cover Assessment through Augmented Visual  
710 Interpretation. *Remote Sensing* 8:807.
- 711 Boschetti, L., S. P. Flasse, and P. A. Brivio. 2004. Analysis of the conflict between omission and  
712 commission in low spatial resolution dichotomic thematic products: The Pareto Boundary. *Remote*  
713 *Sensing of Environment* 91:280–292.
- 714 Breiman, L. 2001. Random Forests. *Machine Learning* 45:5–32.
- 715 Bullock, E. L., S. P. Healey, Z. Yang, P. Oduor, N. Gorelick, S. Omondi, E. Ouko, and W. B. Cohen.  
716 2021. Three Decades of Land Cover Change in East Africa. *Land* 10:150.
- 717 Burke, M., A. Driscoll, D. B. Lobell, and S. Ermon. 2021. Using satellite imagery to understand and  
718 promote sustainable development. *Science* 371.
- 719 Carletto, C., S. Gourlay, and P. Winters. 2015. From Guesstimates to GPStimates: Land Area  
720 Measurement and Implications for Agricultural Analysis. *Journal of African Economies* 24:593–628.
- 721 Carletto, C., S. Savastano, and A. Zezza. 2013. Fact or artifact: The impact of measurement errors on  
722 the farm sizeproductivity relationship. *Journal of Development Economics* 103:254–261.
- 723 Chen, J., J. Chen, A. Liao, X. Cao, L. Chen, X. Chen, C. He, G. Han, S. Peng, M. Lu, W. Zhang, X.  
724 Tong, and J. Mills. 2015. Global land cover mapping at 30 m resolution: A POK-based operational  
725 approach. *ISPRS Journal of Photogrammetry and Remote Sensing* 103:7–27.
- 726 Cohn, D., L. Atlas, and R. Ladner. 1994. Improving generalization with active learning. *Machine*  
727 *Learning* 15:201–221.
- 728 Dark, S. J., and D. Bram. 2007. The modifiable areal unit problem (MAUP) in physical geography.  
729 *Progress in Physical Geography* 31:471–479.

- 730 Davis, K. F., H. I. Koo, J. Dell'Angelo, P. D'Odorico, L. Estes, L. J. Kehoe, M. Kharratzadeh, T.  
731 Kuemmerle, D. Machava, A. de J. R. Pais, N. Ribeiro, M. C. Rulli, and M. Tatlhogo. 2020. Tropical  
732 forest loss enhanced by large-scale land acquisitions. *Nature Geoscience*:1–7.
- 733 Debats, S. R., L. D. Estes, D. R. Thompson, and K. K. Caylor. 2017. Integrating active learning and  
734 crowdsourcing into large-scale supervised landcover mapping algorithms. *PeerJ Preprints*.
- 735 Debats, S. R., D. Luo, L. D. Estes, T. J. Fuchs, and K. K. Caylor. 2016. A generalized computer vision  
736 approach to mapping crop fields in heterogeneous agricultural landscapes. *Remote Sensing of  
737 Environment* 179:210–221.
- 738 Defourny, P., S. Bontemps, N. Bellemans, C. Cara, G. Dedieu, E. Guzzonato, O. Hagolle, J. Inglada, L.  
739 Nicola, T. Rabaute, M. Savinaud, C. Udrouiu, S. Valero, A. Bégué, J.-F. Dejoux, A. El Harti, J.  
740 Ezzahar, N. Kussul, K. Labbassi, V. Lebourgeois, Z. Miao, T. Newby, A. Nyamugama, N. Salh, A.  
741 Shelestov, V. Simonneaux, P. S. Traore, S. S. Traore, and B. Koetz. 2019. Near real-time  
742 agriculture monitoring at national scale at parcel resolution: Performance assessment of the  
743 Sen2-Agri automated system in various cropping systems around the world. *Remote Sensing of  
744 Environment* 221:551–568.
- 745 Desiere, S., and D. Jolliffe. 2018. Land productivity and plot size: Is measurement error driving the  
746 inverse relationship? *Journal of Development Economics* 130:84–98.
- 747 Drusch, M., U. Del Bello, S. Carlier, O. Colin, V. Fernandez, F. Gascon, B. Hoersch, C. Isola, P.  
748 Laberinti, P. Martimort, A. Meygret, F. Spoto, O. Sy, F. Marchese, and P. Bargellini. 2012.  
749 Sentinel-2: ESA's Optical High-Resolution Mission for GMES Operational Services. *Remote  
750 Sensing of Environment* 120:25–36.
- 751 Dwyer, J. L., D. P. Roy, B. Sauer, C. B. Jenkerson, H. K. Zhang, and L. Lymburner. 2018. Analysis  
752 Ready Data: Enabling Analysis of the Landsat Archive. *Remote Sensing* 10:1363.
- 753 Elmes, A., H. Alemohammad, R. Avery, K. Caylor, J. R. Eastman, L. Fishgold, M. A. Friedl, M. Jain,  
754 D. Kohli, J. C. Laso Bayas, D. Lunga, J. L. McCarty, R. G. Pontius, A. B. Reinmann, J. Rogan, L.  
755 Song, H. Stoyanova, S. Ye, Z.-F. Yi, and L. Estes. 2020. Accounting for training data error in  
756 machine learning applied to Earth Observations. *Remote Sensing* 12:1034.
- 757 ESA. (n.d.). ESA CCI LAND COVER S2 prototype Land Cover 20m map of Africa 2016.  
758 <http://2016africalandcover20m.esrin.esa.int/>.
- 759 Estes, L., P. Chen, S. Debats, T. Evans, S. Ferreira, T. Kuemmerle, G. Ragazzo, J. Sheffield, A. Wolf,  
760 E. Wood, and K. Caylor. 2018. A large-area, spatially continuous assessment of land cover map  
761 error and its impact on downstream analyses. *Global Change Biology* 24:322–337.
- 762 Estes, L. D., H. Beukes, B. A. Bradley, S. R. Debats, M. Oppenheimer, A. C. Ruane, R. Schulze, and  
763 M. Tadross. 2013. Projected climate impacts to South African maize and wheat production in 2055:  
764 A comparison of empirical and mechanistic modeling approaches. *Global Change Biology*  
765 19:3762–3774.
- 766 Estes, L. D., D. McRitchie, J. Choi, S. Debats, T. Evans, W. Guthe, D. Luo, G. Ragazzo, R. Zempleni,  
767 and K. K. Caylor. 2016a. A platform for crowdsourcing the creation of representative, accurate  
768 landcover maps. *Environmental Modelling & Software* 80:41–53.

- 769 Estes, L. D., T. Searchinger, M. Spiegel, D. Tian, S. Sickinga, M. Mwale, L. Kehoe, T. Kuemmerle, A.  
770 Berven, N. Chaney, J. Sheffield, E. F. Wood, and K. K. Caylor. 2016b. Reconciling agriculture,  
771 carbon and biodiversity in a savannah transformation frontier. *Phil. Trans. R. Soc. B* 371:20150316.
- 772 Feder, G. 1985. The relation between farm size and farm productivity: The role of family labor,  
773 supervision and credit constraints. *Journal of Development Economics* 18:297–313.
- 774 Forkuor, G., C. Conrad, M. Thiel, T. Ullmann, and E. Zoungrana. 2014. Integration of Optical and  
775 Synthetic Aperture Radar Imagery for Improving Crop Mapping in Northwestern Benin, West  
776 Africa. *Remote Sensing* 6:6472–6499.
- 777 Fourie, A. 2009. Better Crop Estimates in South Africa. ArcUser Online.
- 778 Fritz, S., I. McCallum, C. Schill, C. Perger, L. See, D. Schepaschenko, M. van der Velde, F. Kraxner,  
779 and M. Obersteiner. 2012. Geo-Wiki: An online platform for improving global land cover.  
780 *Environmental Modelling & Software* 31:110–123.
- 781 Fritz, S., L. See, I. McCallum, C. Schill, M. Obersteiner, M. van der Velde, H. Boettcher, P. Havlík,  
782 and F. Achard. 2011. Highlighting continued uncertainty in global land cover maps for the user  
783 community. *Environmental Research Letters* 6:044005.
- 784 Fritz, S., L. See, I. McCallum, L. You, A. Bun, E. Moltchanova, M. Duerauer, F. Albrecht, C. Schill, C.  
785 Perger, P. Havlik, A. Mosnier, P. Thornton, U. Wood-Sichra, M. Herrero, I. Becker-Reshef, C.  
786 Justice, M. Hansen, P. Gong, S. Abdel Aziz, A. Cipriani, R. Cumani, G. Cecchi, G. Conchedda, S.  
787 Ferreira, A. Gomez, M. Haffani, F. Kayitakire, J. Malanding, R. Mueller, T. Newby, A. Nonguierma,  
788 A. Olusegun, S. Ortner, D. R. Rajak, J. Rocha, D. Schepaschenko, M. Schepaschenko, A. Terekhov,  
789 A. Tiangwa, C. Vancutsem, E. Vintrou, W. Wenbin, M. van der Velde, A. Dunwoody, F. Kraxner,  
790 and M. Obersteiner. 2015. Mapping global cropland and field size. *Global Change Biology*  
791 21:1980–1992.
- 792 Fritz, S., L. See, and F. Rembold. 2010. Comparison of global and regional land cover maps with  
793 statistical information for the agricultural domain in Africa. *International Journal of Remote*  
794 *Sensing* 31:2237–2256.
- 795 Fritz, S., L. See, L. You, C. Justice, I. Becker-Reshef, L. Bydekerke, R. Cumani, P. Defourny, K. Erb, J.  
796 Foley, S. Gilliams, P. Gong, M. Hansen, T. Hertel, M. Herold, M. Herrero, F. Kayitakire, J. Latham,  
797 O. Leo, I. McCallum, M. Obersteiner, N. Ramankutty, J. Rocha, H. Tang, P. Thornton, C.  
798 Vancutsem, M. van der Velde, S. Wood, and C. Woodcock. 2013. The need for improved maps of  
799 global cropland. *Eos, Transactions American Geophysical Union* 94:31–32.
- 800 Gibbs, H. K., A. S. Ruesch, F. Achard, M. K. Clayton, P. Holmgren, N. Ramankutty, and J. A. Foley.  
801 2010. Tropical forests were the primary sources of new agricultural land in the 1980s and 1990s.  
802 *Proceedings of the National Academy of Sciences* 107:16732–16737.
- 803 Gorelick, N., M. Hancher, M. Dixon, S. Ilyushchenko, D. Thau, and R. Moore. 2017. Google Earth  
804 Engine: Planetary-scale geospatial analysis for everyone. *Remote Sensing of Environment* 202:18–27.
- 805 Hackman, K. O., P. Gong, and J. Wang. 2017. New land-cover maps of Ghana for 2015 using Landsat  
806 8 and three popular classifiers for biodiversity assessment. *International Journal of Remote Sensing*  
807 38:4008–4021.

- 808 Hamrouni, Y., E. Paillassa, V. Chéret, C. Monteil, and D. Sheeren. 2021. From local to global: A  
809 transfer learning-based approach for mapping poplar plantations at national scale using Sentinel-2.  
810 *ISPRS Journal of Photogrammetry and Remote Sensing* 171:76–100.
- 811 Houborg, R., and M. McCabe. 2018. Daily Retrieval of NDVI and LAI at 3 m Resolution via the  
812 Fusion of CubeSat, Landsat, and MODIS Data. *Remote Sensing* 10:890.
- 813 Kansanga, M., P. Andersen, D. Kpienbaareh, S. Mason-Renton, K. Atuoye, Y. Sano, R. Antabe, and I.  
814 Luginaah. 2019. Traditional agriculture in transition: Examining the impacts of agricultural  
815 modernization on smallholder farming in Ghana under the new Green Revolution. *International*  
816 *Journal of Sustainable Development & World Ecology* 26:11–24.
- 817 Kehoe, L., A. Romero-Muñoz, L. Estes, H. Kreft, E. Polaina, and T. Kuemmerle. 2017. Nature at risk  
818 under future agricultural expansion and intensification. *Nature Ecology and Evolution* 1:1129–1135.
- 819 Kerner, H., G. Tseng, I. Becker-Reshef, C. Nakalembe, B. Barker, B. Munshell, M. Paliyam, and M.  
820 Hosseini. 2020. Rapid Response Crop Maps in Data Sparse Regions. arXiv:2006.16866 [cs, eess].
- 821 Lebourgeois, V., S. Dupuy, É. Vintrou, M. Ameline, S. Butler, and A. Bégué. 2017. A Combined  
822 Random Forest and OBIA Classification Scheme for Mapping Smallholder Agriculture at Different  
823 Nomenclature Levels Using Multisource Data (Simulated Sentinel-2 Time Series, VHRS and DEM).  
824 *Remote Sensing* 9:259.
- 825 Lesiv, M., S. Fritz, I. McCallum, N. Tsendbazar, M. Herold, J.-F. Pekel, M. Buchhorn, B. Smets, and  
826 R. Van De Kerchove. 2017, November. Evaluation of ESA CCI prototype land cover map at 20m.  
827 Monograph, <http://pure.iiasa.ac.at/id/eprint/14979/>.
- 828 Lesiv, M., J. C. Laso Bayas, L. See, M. Duerauer, D. Dahlia, N. Durando, R. Hazarika, P. Kumar  
829 Sahariah, M. Vakolyuk, V. Blyshchyk, A. Bilous, A. Perez-Hoyos, S. Gengler, R. Prestele, S. Bilous,  
830 I. ul H. Akhtar, K. Singha, S. B. Choudhury, T. Chetri, Ž. Malek, K. Bungnamei, A. Saikia, D.  
831 Sahariah, W. Narzary, O. Danylo, T. Sturn, M. Karner, I. McCallum, D. Schepaschenko, E.  
832 Moltchanova, D. Fraisl, I. Moorthy, and S. Fritz. 2019. Estimating the global distribution of field  
833 size using crowdsourcing. *Global Change Biology* 25:174–186.
- 834 Lesiv, M., L. See, J. Laso Bayas, T. Sturn, D. Schepaschenko, M. Karner, I. Moorthy, I. McCallum, and  
835 S. Fritz. 2018. Characterizing the spatial and temporal availability of very high resolution satellite  
836 imagery in Google Earth and Microsoft Bing maps as a source of reference data. *Land* 7:118.
- 837 Levin, G. 2006. Farm size and landscape composition in relation to landscape changes in Denmark.  
838 *Geografisk Tidsskrift-Danish Journal of Geography* 106:45–59.
- 839 Licker, R., M. Johnston, J. A. Foley, C. Barford, C. J. Kucharik, C. Monfreda, and N. Ramankutty.  
840 2010. Mind the gap: How do climate and agricultural management explain the ‘yield gap’ of  
841 croplands around the world? *Global Ecology and Biogeography* 19:769–782.
- 842 Lobell, D. B., K. G. Cassman, and C. B. Field. 2009. Crop Yield Gaps: Their Importance, Magnitudes,  
843 and Causes. *Annual Review of Environment and Resources* 34:179–204.
- 844 Ma, L., Y. Liu, X. Zhang, Y. Ye, G. Yin, and B. A. Johnson. 2019. Deep learning in remote sensing  
845 applications: A meta-analysis and review. *ISPRS Journal of Photogrammetry and Remote Sensing*

- 846 152:166–177.
- 847 Maxwell, A. E., T. A. Warner, and F. Fang. 2018. Implementation of machine-learning classification in  
848 remote sensing: An applied review. *International Journal of Remote Sensing* 39:2784–2817.
- 849 McCabe, M. F., M. Rodell, D. E. Alsdorf, D. G. Miralles, R. Uijlenhoet, W. Wagner, A. Lucieer, R.  
850 Houborg, N. E. C. Verhoest, T. E. Franz, J. Shi, H. Gao, and E. F. Wood. 2017. The future of  
851 Earth observation in hydrology. *Hydrology and Earth System Sciences* 21:3879–3914.
- 852 Mellor, A., S. Boukir, A. Haywood, and S. Jones. 2015. Exploring issues of training data imbalance  
853 and mislabelling on random forest performance for large area land cover classification using the  
854 ensemble margin. *ISPRS Journal of Photogrammetry and Remote Sensing* 105:155–168.
- 855 Morris, M., and D. Byerlee. 2009. *Awakening Africa’s Sleeping Giant*. World Bank and FAO,  
856 Washington, DC.
- 857 Mueller, N. D., J. S. Gerber, M. Johnston, D. K. Ray, N. Ramankutty, and J. A. Foley. 2012. Closing  
858 yield gaps through nutrient and water management. *Nature* 490:254–257.
- 859 Neubert, P., and P. Protzel. 2014. Compact Watershed and Preemptive SLIC: On Improving Trade-offs  
860 of Superpixel Segmentation Algorithms. Pages 996–1001 2014 22nd International Conference on  
861 Pattern Recognition. IEEE, Stockholm, Sweden.
- 862 Olofsson, P., G. M. Foody, M. Herold, S. V. Stehman, C. E. Woodcock, and M. A. Wulder. 2014. Good  
863 practices for estimating area and assessing accuracy of land change. *Remote Sensing of  
864 Environment* 148:42–57.
- 865 Olofsson, P., G. M. Foody, S. V. Stehman, and C. E. Woodcock. 2013. Making better use of accuracy  
866 data in land change studies: Estimating accuracy and area and quantifying uncertainty using  
867 stratified estimation. *Remote Sensing of Environment* 129:122–131.
- 868 Openshaw, S., and P. J. Taylor. 1979. A million or so correlation coefficients: Three experiments on  
869 the modifiable areal unit problem. *Statistical applications in the spatial sciences* 21:127–144.
- 870 Persello, C., V. A. Tolpekin, J. R. Bergado, and R. A. de By. 2019. Delineation of agricultural fields in  
871 smallholder farms from satellite images using fully convolutional networks and combinatorial  
872 grouping. *Remote Sensing of Environment* 231:111253.
- 873 PlanetTeam. 2018. Planet application program interface: In space for life on Earth.  
874 <https://api.planet.com>, San Francisco, CA.
- 875 Pontius, R. G., and K. Si. 2014. The total operating characteristic to measure diagnostic ability for  
876 multiple thresholds. *International Journal of Geographical Information Science* 28:570–583.
- 877 Qiu, S., Z. Zhu, and C. E. Woodcock. 2020. Cirrus clouds that adversely affect Landsat 8 images:  
878 What are they and how to detect them? *Remote Sensing of Environment* 246:111884.
- 879 Rodriguez-Galiano, V. F., B. Ghimire, J. Rogan, M. Chica-Olmo, and J. P. Rigol-Sanchez. 2012. An  
880 assessment of the effectiveness of a random forest classifier for land-cover classification. *ISPRS  
881 Journal of Photogrammetry and Remote Sensing* 67:93–104.

- 882 Roy, D. P., H. Huang, R. Houborg, and V. S. Martins. 2021. A global analysis of the temporal  
883 availability of PlanetScope high spatial resolution multi-spectral imagery. *Remote Sensing of*  
884 *Environment* 264:112586.
- 885 Rulli, M. C., and P. D’Odorico. 2014. Food appropriation through large scale land acquisitions.  
886 *Environmental Research Letters* 9:064030.
- 887 Samberg, L. H., J. S. Gerber, N. Ramankutty, M. Herrero, and P. C. West. 2016. Subnational  
888 distribution of average farm size and smallholder contributions to global food production.  
889 *Environmental Research Letters* 11:124010.
- 890 Searchinger, T. D., L. Estes, P. K. Thornton, T. Beringer, A. Notenbaert, D. Rubenstein, R. Heimlich,  
891 R. Licker, and M. Herrero. 2015. High carbon and biodiversity costs from converting Africa’s wet  
892 savannahs to cropland. *Nature Climate Change* 5:481–486.
- 893 Searchinger, T., R. Waite, C. Hanson, J. Ranganathan, P. Dumas, E. Matthews, and C. Klirs. 2019.  
894 Creating a sustainable food future: A menu of solutions to feed nearly 10 billion people by 2050.  
895 Final report. WRI.
- 896 Stehman, S. V., and G. M. Foody. 2019. Key issues in rigorous accuracy assessment of land cover  
897 products. *Remote Sensing of Environment* 231:111199.
- 898 Sulla-Menashe, D., J. M. Gray, S. P. Abercrombie, and M. A. Friedl. 2019. Hierarchical mapping of  
899 annual global land cover 2001 to present: The MODIS Collection 6 Land Cover product. *Remote*  
900 *Sensing of Environment* 222:183–194.
- 901 Tong, X., M. Brandt, P. Hiernaux, S. Herrmann, L. V. Rasmussen, K. Rasmussen, F. Tian, T.  
902 Tagesson, W. Zhang, and R. Fensholt. 2020. The forgotten land use class: Mapping of fallow fields  
903 across the Sahel using Sentinel-2. *Remote Sensing of Environment* 239:111598.
- 904 Tuia, D., M. Volpi, L. Copa, M. Kanevski, and J. Munoz-Mari. 2011. A Survey of Active Learning  
905 Algorithms for Supervised Remote Sensing Image Classification. *IEEE Journal of Selected Topics in*  
906 *Signal Processing* 5:606–617.
- 907 Van Vliet, N., O. Mertz, T. Birch-Thomsen, and B. Schmook. 2013. Is There a Continuing Rationale  
908 for Swidden Cultivation in the 21st Century? *Human Ecology* 41:1–5.
- 909 Visvalingam, M., and J. D. Whyatt. 1993. Line generalisation by repeated elimination of points. *The*  
910 *Cartographic Journal* 30:46–51.
- 911 Waldner, F., and F. I. Diakogiannis. 2020. Deep learning on edge: Extracting field boundaries from  
912 satellite images with a convolutional neural network. *Remote Sensing of Environment* 245:111741.
- 913 Waldner, F., A. Schucknecht, M. Lesiv, J. Gallego, L. See, A. Pérez-Hoyos, R. d’Andrimont, T. de  
914 Maet, J. C. L. Bayas, S. Fritz, O. Leo, H. Kerdiles, M. Díez, K. Van Tricht, S. Gilliams, A.  
915 Shelestov, M. Lavreniuk, M. Simões, R. Ferraz, B. Bellón, A. Bégué, G. Hazeu, V. Stonacek, J.  
916 Kolomaznik, J. Misurec, S. R. Verón, D. de Abelleira, D. Plotnikov, L. Mingyong, M. Singha, P.  
917 Patil, M. Zhang, and P. Defourny. 2019. Conflation of expert and crowd reference data to validate  
918 global binary thematic maps. *Remote Sensing of Environment* 221:235–246.



- 919 Wilson, A. M., and W. Jetz. 2016. Remotely Sensed High-Resolution Global Cloud Dynamics for  
920 Predicting Ecosystem and Biodiversity Distributions. *PLOS Biology* 14:e1002415.
- 921 Wulder, M. A., J. C. White, T. R. Loveland, C. E. Woodcock, A. S. Belward, W. B. Cohen, E. A.  
922 Fosnight, J. Shaw, J. G. Masek, and D. P. Roy. 2016. The global Landsat archive: Status,  
923 consolidation, and direction. *Remote Sensing of Environment* 185:271–283.
- 924 Xiong, J., P. S. Thenkabail, J. C. Tilton, M. K. Gumma, P. Teluguntla, A. Oliphant, R. G. Congalton,  
925 K. Yadav, and N. Gorelick. 2017. Nominal 30-m Cropland Extent Map of Continental Africa by  
926 Integrating Pixel-Based and Object-Based Algorithms Using Sentinel-2 and Landsat-8 Data on  
927 Google Earth Engine. *Remote Sensing* 9:1065.
- 928 Ye, S., R. G. Pontius, and R. Rakshit. 2018. A review of accuracy assessment for object-based image  
929 analysis: From per-pixel to per-polygon approaches. *ISPRS Journal of Photogrammetry and*  
930 *Remote Sensing* 141:137–147.
- 931 Yizong Cheng. 1995. Mean shift, mode seeking, and clustering. *IEEE Transactions on Pattern Analysis*  
932 *and Machine Intelligence* 17:790–799.
- 933 Zeng, Z., L. Estes, A. D. Ziegler, A. Chen, T. Searchinger, F. Hua, K. Guan, A. Jintrawet, and E. F.  
934 Wood. 2018. Highland cropland expansion and forest loss in Southeast Asia in the twenty-first  
935 century. *Nature Geoscience* 11:556–562.
- 936 Zhang, X., L. Liu, X. Chen, Y. Gao, S. Xie, and J. Mi. 2021. GLC\_FCS30: Global land-cover product  
937 with fine classification system at 30 m using time-series Landsat imagery. *Earth System Science*  
938 *Data* 13:2753–2776.
- 939 Zhang, Y., B. Guindon, and J. Cihlar. 2002. An image transform to characterize and compensate for  
940 spatial variations in thin cloud contamination of Landsat images. *Remote Sensing of Environment*  
941 82:173–187.
- 942 Zhu, Z., and C. E. Woodcock. 2012. Object-based cloud and cloud shadow detection in Landsat  
943 imagery. *Remote Sensing of Environment* 118:83–94.